Stony Brook University

Structure Assignments to Excited States of Heavy Nuclei from Lifetime Information

A Dissertation Presented

by

Alin Vasile Costin

to

The Graduate School

in Partial Fulfillment of the

Requirements

for the Degree of

Doctor of Philosophy

in

Physics

Stony Brook University

May 2008

Stony Brook University

The Graduate School

Alin Vasile Costin

We, the dissertation committee for the above candidate for the

Doctor of Philosophy degree,

hereby recommend acceptance of the dissertation.

Dr. Gene D. Sprouse - Dissertation Advisor
Professor of Physics, Department of Physics and Astronomy

Dr. Thomas T. S. Kuo - Chairperson of Defense
Professor of Physics, Department of Physics and Astronomy

Dr. Clark McGrew
Associate Professor of Physics, Department of Physics and Astronomy

Dr. Norbert Pietralla
Professor of Physics
Institut für Kernphysik, Technische Universität Darmstadt

This dissertation is accepted by the Graduate School

Lawrence Martin
Dean of the Graduate School

Abstract of the Dissertation

Structure Assignments to Excited States of Heavy Nuclei from Lifetime Information

by

Alin Vasile Costin

Doctor of Philosophy

in

Physics

Stony Brook University

2008

The discovery of the neutron in 1932 led way to a series of successful nuclear models. The first of them, the Liquid Drop Model, describes a few basic nuclear properties such as binding energy and level density. It was followed by what is today considered the fundamental microscopic nuclear model, the Shell Model, which suggests that protons and neutrons move in well defined orbits, similar to electrons in atoms. With the development of nuclear structure in medium and heavy nuclei far from closed shells, more reliable approaches such as collective models have been proposed. They bypass the shell model by stressing the macroscopic motions,

rotations or vibrations, and excitations of a nucleus having a specific shape or by exploiting the dynamical symmetry structure of nuclei. One class is referred to as geometrical models and the other as algebraic models, respectively. The derivation of the Bohr Hamiltonian, a part of the Bohr-Mottelson geometrical model, is presented at the beginning of Chapter 1. The Bohr Hamiltonian is the starting point for the critical point symmetry $X(5)$. The development of the $X(5)$ model was prompted by evidence of nuclei displaying shape phase transition properties between the vibrational and rotational benchmarks of nuclear structure. The second part of Chapter 1 deals with the Confined β-soft Rotor Model (CBS), an interpolation between the spherical-to-deformed critical point approximation $X(5)$ and the rigid rotor limit. After looking into the analytical formulation of the CBS, some predictions and comparisons with experiment are given. A key prediction is the increase in average deformation of nuclei with angular momentum, phenomenon referred to as centrifugal stretching. This phenomenon is observed in nuclei close to the phase transition region. Pushing the observations of centrifugal stretching toward the region of strongly deformed nuclei is the intended purpose behind this Thesis work.

Absolute transition rates provide an important insight into the properties of nuclear many-body systems. They are sensitive to fundamental interactions, like the electro-weak interaction in β- and γ-decay processes or the strong interaction in α-decay and fis-

sion processes, through the wave functions of the nuclear states involved in the transition. In this context, a major effort is placed in the measurement of lifetimes of these nuclear states, as one of the ways of determining the transition rates. The range over which lifetimes have been measured spans more than 40 orders of magnitude, starting from the very long lifetime of the α-emitter ^{209}Bi ($\tau = 2.0 \times 10^{19}$ y) to very short decay processes, such as the α-decay of the ^{8}Be ground state ($\tau = 1.0 \times 10^{-19}$ s). Due to this large span, different timing methods were developed which cover certain time ranges. Chapter 2 and 3 summarize two direct timing techniques, delayed coincidence timing and recoil distance Doppler shift timing respectively, both of which were used in experiments connected to the purpose of this Thesis. The principle of the delayed coincidence timing consists of measuring the distribution of time delays between the formation and subsequent decay of the nuclear state of interest. The two most common analysis methods of delayed coincidence data, the slope method and the centroid shift method are summarized. The principle of the recoil distance Doppler shift timing consists of measuring the change in intensities of unshifted and Doppler shifted peaks with changing distance between a target and a stopper. The description of the plunger and the general formulation of the differential decay curve method for analysis of recoil distance data are also given in Chapter 3.

New, more precise lifetime measurements were performed on

ground state levels of ^{168}Hf and ^{170}Hf for a precision test of the CBS rotor model. Their experimental details, data analysis and results are presented in Chapter 4. The discussion of these results represents the content of Chapter 5.

Contents

List of Figures

List of Tables

Acknowledgements

First and foremost, I would like to thank my dissertation advisor Norbert Pietralla, whose passion for nuclear physics is contagious. Not only did he guide my first steps as a researcher, but he also gave me the opportunity to experience a great country, Germany, by taking me along during his latest career whereabouts.

Then, I would like to thank Georgi Rainovski, Norbert's postdoc for two years, for his tremendous help with everything from experimental work to data analysis, computer related issues and physics discussions.

This thesis is based on experimental work so help from the Nuclear Structure Laboratory staff, in particular from R. Lefferts, A. Lipski and B. Gutschow, and WNSL of Yale University staff for providing excellent beams and and technical support, is gratefully acknowledged. I am also indebted to all of Norbert's students, graduate and undergraduate, who helped me by taking experimental shifts for data collection.

Finally, I must thank my official advisor, Gene Sprouse, for kindly agreeing to take on this role given the circumstances and for the financial help he provided while I was working abroad.

Chapter 1

The Confined β-soft Rotor Model

The content of this chapter is largely based on material taken from Refs. [1, 2, 3].

1.1 Introduction

The Liquid Drop Model (LDM) has been the first successful nuclear model. Formulated by N. Bohr [4, 5], the LDM treats the nucleus as a drop of incompressible fluid made of nucleons held together by the strong force. The fundamental modes of nuclear excitation correspond to collective types of motion, such as surface oscillations and elastic vibrations. The LDM has found numerous applications in the theory of nuclear reactions. The model gives an explanation of the rapid increase of level density with increasing excitation of the nucleus and also accounts for certain static properties of the nucleus. Thus, the binding energy of the nuclear droplet is expressed analytically as a sum of five terms in the semi-empirical mass formula of Weizsäcker. An important application of the Weizsäcker formula was in the analysis of nuclear

fission [6, 7]. While successful in predicting the binding energy of heavier nuclei, the formula fails to deliver accurate results for lighter nuclei because the LDM does not consider the internal shell structure of nuclei.

The Shell Model (SM) was developed independently in the late 1940s by M. G. Mayer [8] and J. H. D. Jensen [9, 10, 11] and is now considered the fundamental microscopic nuclear model phenomenologically using the protons and neutrons as the relevant degrees of freedom. Experimental evidence that the nucleons, like electrons in atoms, move in well defined orbits was the origin of the SM. This is a surprising finding because it suggests that nucleons move rather freely in the interior of the nucleus despite the very strong nuclear force. The SM has proven very successful in describing, from a microscopic point of view, far more properties of nuclei with few valence nucleons, than the LDM: energy levels, electromagnetic transition probabilities, quadrupole moments, beta-decay rates, reaction cross-sections etc. It provides a well-defined procedure, with only a few basic ingredients (some single-particle energy levels and the residual interaction), for the calculation of these observables. Unfortunately, the use of the shell model is, in practice, severely limited. Except for very light nuclei and those very near closed shells, SM calculations involve matrices with sizes that rapidly become enormous, due to increasing valence nucleons or model space. Even for a few valence nucleons in several j orbits, one can construct hundreds of states of a given J^π value and the results are difficult to interpret physically. Nevertheless, since the SM is the only broadly applicable microscopic model available, it is the standard against which others are compared.

With the development of nuclear structure in medium and heavy nuclei far from closed shells where the SM is either intractable or unreliable, new theoretical approaches have been developed. A significant class represents the *geometrical* or *collective* models which bypass the shell model by stressing the macroscopic motions, rotations or vibrations, and excitations of a nucleus having a specific *shape*. It is an undeniable experimental fact, *e.g.* the quadrupole moments observed for many nuclei are too large to be accounted for in terms of individual nucleons, that many nuclei show evidence of collective behavior that seems to contradict the concept of a shell structure. Despite all the predictive power and success of collective models, it was a critical issue whether or not such structures can be derived microscopically from the shell model. Indeed, it was demonstrated in the early 1960s that macroscopic collectivity could result from the shell model with appropriate realistic residual interactions. The method is called Random Phase Approximation (RPA). The collective model of Bohr and Mottelson [1, 12, 13, 14] will be briefly discussed in the next section, as a basis for the subsequent discussion of the Confined β-soft Rotor Model (CBS) [2] which is the underlying model behind this thesis work.

Another class of models developed more recently takes a different approach to collective behavior in nuclei. It exploits the dynamical symmetry structure of nuclei and utilizes powerful group theoretical techniques to obtain many nuclear properties by simple algebraic manipulations. Of these, the most tested and successful to date has been the Interacting Boson Approximation (IBA). IBA was proposed by Arima and Iachello in 1974 [15] and further developed in the following years [16, 17, 18]. The existence and role of symmetries in

the IBA framework represent its most unique and characteristic feature. There are three of these symmetries, called *dynamical symmetries*, that are physically interesting, known by the labels $U(5)$, $SU(3)$ and $O(6)$. Their description is simple and analytic, they have clear geometrical relationships and physical interpretations [$U(5)$ corresponds to spherical harmonic vibrator, $SU(3)$ to axially symmetric rotor and $O(6)$ to axially asymmetric shapes] and their predictions depend on a minimum of parameters.

It should be stressed that IBA is a model for collective behavior. One usually refers to collective models of the Bohr-Mottelson type as "geometric" models and those of the group theory-based class as "algebraic" models. In this sense, IBA provides an alternative to the situation in which a number of geometrical models, each applicable to a different structure, would be applied according to the empirically observed characteristics. Despite its phenomenological character, IBA has a microscopic aspect since the key ingredient of its formalism is the number of valence nucleons available and a substantial part of the predicted structural changes across a major shell arise automatically from the change in this number.

Although in general the analytical approach fails to describe nuclei with structures intermediate between two symmetries, the symmetries act as benchmarks for more detailed calculations. Moreover, the critical point symmetries with exact analytical solutions $E(5)$ [19] and $X(5)$ [20] have been identified by Iachello at phase transition regions between $U(5)$ and $O(6)$, and $U(5)$ and $SU(3)$ dynamical symmetries, respectively.

The three classes of models shortly introduced here - shell, geometric and

algebraic - are as many tools with which one can solve basic problems of nuclear structure. Although they are different in certain important details, they reflect three approaches to nuclear structure that emphasize complementary aspects of nuclear phenomena.

1.2 Nuclear Collectivity

A derivation and thorough understanding of the Bohr Hamiltonian [1] which is the starting point to the CBS model will be attempted in this section.

The importance of taking into account the collective aspects of the nuclear structure was mentioned in the previous section. The various collective properties of a nucleus are an effect of a deformable surface. It is more appropriate to describe these properties using a Hamiltonian expressed in terms of the macroscopic coordinates of the system, such as radius, mass and volume. In the following, the Hamiltonian of the nuclear surface will be derived using the classical approach of the theory of nuclear surface oscillations. The quantum mechanical equivalent will be then obtained by means of quantization.

The surface of the nucleus away from its equilibrium spherical shape, in polar coordinates, may be described in the following way:

$$R(\theta,\phi;t) = R_0 \left\{ 1 + \sum_{\lambda,\mu} \alpha_{\lambda\mu}(t) Y_{\lambda\mu}(\theta,\phi) \right\}, \tag{1.1}$$

where R_0 is the equilibrium radius, the expansion parameters $\alpha_{\lambda\mu}(t)$ are the coordinates which describe the deformation of the nuclear surface and $Y_{\lambda\mu}(\theta,\phi)$ are the normalized spherical harmonics of order λ,μ, with $2\lambda+1$ values of μ:

$-\lambda$, $-\lambda+1$,..., $\lambda-1$, λ. Since $R(\theta,\phi;t)$ is real, using the property of spherical harmonics that

$$Y^*_{\lambda\mu}(\theta,\phi) = (-1)^\mu Y_{\lambda,-\mu}(\theta,\phi), \tag{1.2}$$

the number of independent shape parameters $\alpha_{\lambda\mu}(t)$ becomes smaller according to

$$\alpha_{\lambda\mu}(t) = (-1)^\mu \alpha^*_{\lambda,-\mu}(t). \tag{1.3}$$

The change in both kinetic and potential energy of the nucleus is related to the nuclear shape: nucleons move from a location to another and the potential energy increases or decreases when a change of shape occurs. As a result, the energy associated with oscillatory motion may be discussed in terms of variations in time in the shape parameters $\alpha_{\lambda\mu}(t)$ and they also become the appropriate canonical variables of motion, rather than, for example, the coordinates specifying the position of each nucleon. For small $\alpha_{\lambda\mu}(t)$, the kinetic energy of deformation takes the form

$$T = \frac{1}{2}\sum_{\lambda,\mu} B_\lambda \left|\dot{\alpha}_{\lambda\mu}\right|^2, \tag{1.4}$$

where B_λ plays a role equivalent to mass from ordinary kinetic energy. For an incompressible nucleus of constant density ρ_0, assuming nuclear matter to have irrotational flow,

$$B_\lambda = \frac{\rho_0 R_0^5}{\lambda}. \tag{1.5}$$

The associated potential energy is given by

$$V = \frac{1}{2}\sum_{\lambda,\mu} C_\lambda \left|\alpha_{\lambda\mu}\right|^2, \tag{1.6}$$

where C_λ is connected to the surface and Coulomb energies of the nucleus from LDM by (Ref. [14], p. 660)

$$C_\lambda = \frac{1}{4\pi}(\lambda-1)(\lambda+2)\alpha_2 A_{2/3} - \frac{3}{2\pi}\frac{\lambda-1}{2\lambda+1}\alpha_3\frac{Z(Z-1)}{A_{1/3}}, \tag{1.7}$$

with α_2 and α_3 the surface and Coulomb energy parameters of the Weizsäcker formula (Ref. [21], p. 140).

The Hamiltonian of the nuclear surface, for an excitation of order λ, takes the form

$$H_\lambda = T + V = \sum_\mu \left(\frac{B_\lambda}{2}\left|\dot{\alpha}_{\lambda\mu}\right|^2 + \frac{C_\lambda}{2}\left|\alpha_{\lambda\mu}\right|^2 \right). \tag{1.8}$$

Analysis of excitations of order zero and one will not be included in the present discussion. Monopole oscillations ($\lambda = 0$) involve only variations in size without changes to the overall shape while dipole oscillations ($\lambda = 1$) represent just translations of the nucleus center of mass relative to a fixed reference frame. The really interesting physical case is the quadrupole oscillation ($\lambda = 2$). This degree of freedom is capable of exhibiting both rotational and vibrational separations in kinetic energy. Figure 1.1 depicts the above mentioned collective modes. For small values of α, deformations of order $\lambda = 2$ represent an ellipsoid oriented randomly in space. Since the orientation is immaterial as far as the intrinsic nuclear shape is concerned, it is convenient to characterize the deformation by three Euler angles, $(\theta_i) = (\theta_1, \theta_2, \theta_3) = (\theta, \varphi, \psi)$, specifying the orientation of the ellipsoid and two internal parameters determining its shape, instead of the five $\alpha_{2\mu}$ coordinates. This may be expressed formally by transforming the coordinate system K to one fixed with the nucleus, K' (θ, φ represent the polar angles of the z'-axis in the K-system, while $\theta, \pi - \psi$ are

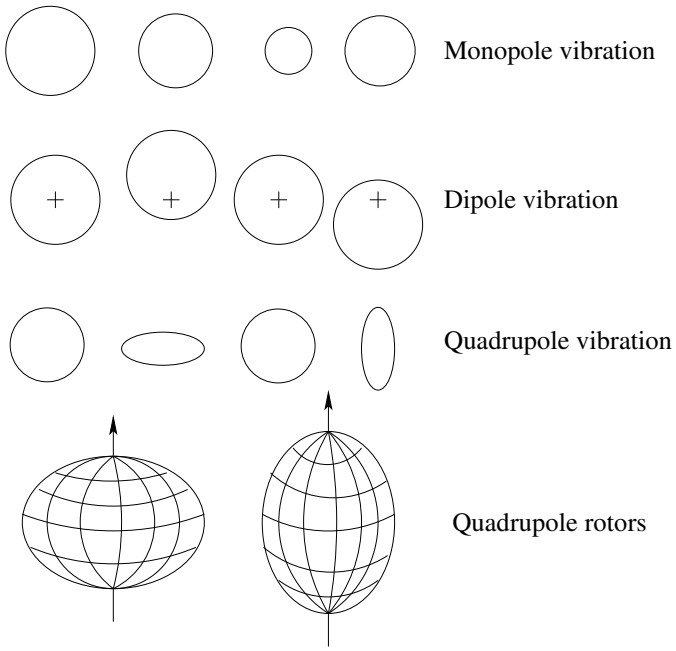

Figure 1.1: *Schematic illustration of several collective oscillation modes. While it would be difficult to represent quadrupole rotations, the two equilibrium shapes of quadrupole rotors are shown in the last row: oblate on the left, and prolate rotor on the right. The rotation takes place around an axis perpendicular to the symmetry axis.*

the polar angles of the z-axis in the K'-system). The deformation defined by $\alpha_{2\mu}$ in K is given in $K^{'}$ by the coefficients

$$a_{2\nu} = \sum_{\mu=-2}^{2} \alpha_{2\mu} D^2_{\mu\nu}(\theta_i), \tag{1.9}$$

where $D^2_{\mu\nu}(\theta_i)$ are the unitary rotation matrices of order 2 (see [21], p. 399), also known as Wigner D-matrices. Since there are only two degrees of freedom left, the body-fixed shape parameters $a_{2\nu}$ have the following properties

$$a_{2,-1} = a_{2,1} = 0 \qquad a_{2,-2} = a_{2,2}\ . \tag{1.10}$$

In the remainder of the analysis we drop the index 2. Taking the inverse of Eq. (1.9) we obtain

$$\alpha_\mu = \sum_{\nu=-2}^{2} a_\nu D^*_{\mu\nu}(\theta_i). \tag{1.11}$$

Instead of the two nonvanishing intrinsic deformation variables a_0 and a_2, it is convenient to use the Hill-Wheeler variables β and γ, defined by the relations

$$a_0 = \beta \cos\gamma \qquad a_{-2} = a_2 = \frac{1}{\sqrt{2}} \beta \sin\gamma \ . \tag{1.12}$$

From the definitions given by Eq. (1.12), it can be seen that the parameter β provides a measure of the extent of deformation and γ, of the departure from axial symmetry. There are different conventions for the ranges of the β and γ variables. The most used one is the Lund convention in which $\beta \geq 0$ and $-120^\circ \leq \gamma \leq -60^\circ$ if the rotation is around the largest axis, $-60^\circ \leq \gamma \leq 0^\circ$ if the rotation is around the intermediate axis and $0^\circ \leq \gamma \leq 60^\circ$ if the rotation is around the smallest axis. An alternate convention is that γ ranges from 0° (axially symmetric) to 30° (maximum axial asymmetry) and that prolate nuclei have $\beta > 0$, while oblate nuclei have $\beta < 0$. The relation between β, γ and the nuclear radii can be seen in the increments of the three axes of the ellipsoid given by

$$\delta R_\kappa = \sqrt{\frac{5}{4\pi}} \ \beta \ R_0 \ \cos\left(\gamma - \kappa \frac{2\pi}{3}\right), \tag{1.13}$$

where $\kappa = 1, 2, 3$ for the $x^{'}$, $y^{'}$ and $z^{'}$ axes of the $K^{'}$ coordinate system. The five shape and angular coordinates β, γ, θ_i will be referred to as β_μ. This set is not unique. A given deformation α_μ only specifies the three symmetry planes of the ellipsoid, but the labeling of the intrinsic axes is arbitrary. The

Hamiltonian and the wave functions must be invariant with respect to the symmetry operations that correspond to a relabeling of the intrinsic axes.

By differentiating Eq. (1.11) with respect to time

$$\dot{\alpha}_\mu = \sum_\nu \dot{a}_\nu D^*_{\mu\nu}(\theta_i) + \sum_{\nu,j} a_\nu \dot{\theta}_j \frac{\partial}{\partial \theta_j} D^*_{\mu\nu}(\theta_i) \tag{1.14}$$

and introducing $\dot{\alpha}_\mu$ in Eq. (1.4), the kinetic energy splits into three terms. The term quadratic in $\dot{a}_\nu$ represents vibrations by which the ellipsoid changes its shape, but retains its orientation and is therefore the vibrational energy of the oscillations. The term quadratic in $\dot{\theta}_i$ represents a rotation of the ellipsoid without change of shape and is the rotational energy of the oscillations. It can be shown from the properties of the $D_{\mu\nu}$-functions and their derivatives that the third term in $\dot{a}_\nu \dot{\theta}_i$ vanishes. We may thus write

$$T = T_{vib} + T_{rot} \tag{1.15}$$

with

$$T_{vib} = \frac{1}{2}\, B \sum_\nu |\dot{a}_\nu|^2 = \frac{1}{2}\, B \left(\dot{\beta}^2 + \beta^2 \dot{\gamma}^2\right) \tag{1.16}$$

easily calculated due to the unitary character of $D_{\mu\nu}$, and

$$T_{rot} = \frac{1}{2} \sum_\kappa \mathcal{I}_\kappa(\beta,\gamma)\omega_\kappa^2 \tag{1.17}$$

(see [1], p.12, for a more detailed derivation of T_{rot}) where $\mathcal{I}_\kappa$ are the moments of inertia given by

$$\mathcal{I}_\kappa(\beta,\gamma) = 4B\beta^2 \sin^2\left(\gamma - \kappa\frac{2\pi}{3}\right) \tag{1.18}$$

and

$$\omega_\kappa = \sum_j \omega_{\kappa j}\dot{\theta}_j \tag{1.19}$$

denote the components of the angular velocity on the three intrinsic axes of the ellipsoid. With our choice of rotations mentioned before, the matrix elements $\omega_{\kappa j}$ are

$$\begin{pmatrix} \sin\psi & -\cos\psi & 0 \\ \sin\theta\cos\psi & \sin\theta\sin\psi & \cos\theta \\ 0 & 0 & 1 \end{pmatrix} . \tag{1.20}$$

The rotational energy may also be written as

$$T_{rot} = \frac{1}{2}\sum_{\kappa}\frac{\mathcal{M}_{\kappa}^2}{\mathcal{I}_{\kappa}} , \tag{1.21}$$

where $\mathcal{M}_{\kappa}$ are the projections of the angular momentum on the intrinsic axes of the oscillating nucleus. By comparing (1.17) with (1.21), one observes that

$$\mathcal{M}_{\kappa} = \mathcal{I}_{\kappa}\omega_{\kappa} . \tag{1.22}$$

The potential energy of deformation takes the form

$$V = \frac{1}{2}\, C\sum_{\nu}|a_{\nu}|^2 = \frac{1}{2}\, C\beta^2 . \tag{1.23}$$

With this last result it is possible now to write the classical Hamiltonian of the nuclear surface in the new coordinates β_{μ}

$$H_s = \frac{1}{2}\, B\left(\dot{\beta}^2 + \beta^2\dot{\gamma}^2\right) + \frac{1}{2}\sum_{\kappa}\frac{\mathcal{M}_{\kappa}^2}{\mathcal{I}_{\kappa}} + \frac{1}{2}\, C\beta^2 . \tag{1.24}$$

It has been shown by Podolsky [22] that the quantization rule is not sufficient to obtain the kinetic energy operator from the classical Hamiltonian. To construct the correct Schrödinger equation in an arbitrary set of coordinates, the Laplace-Beltrami operator multiplied with $-\hbar^2/2$ has to be used as the appropriate form for the quantum mechanical kinetic energy operator. The

potential energy V is not a function of momenta and will therefore be identical with its classical form. The Hamiltonian of the nuclear surface now takes the form

$$H_s = T + V = -\frac{\hbar^2}{2}\sum_{\mu\nu} g^{-1/2}\frac{\partial}{\partial\beta_\mu}g^{1/2}g^{\mu\nu}\frac{\partial}{\partial\beta_\nu} + V \ , \tag{1.25}$$

where g is the determinant of the 5-dimensional metric tensor $(g)_{\mu\nu}$ defined by

$$\mathrm{d}s^2 = \sum_{\mu\nu} g_{\mu\nu}\mathrm{d}\beta_\mu\mathrm{d}\beta_\nu = 2T\mathrm{d}t^2 \ , \tag{1.26}$$

and $g^{\mu\nu} = (g^{-1})_{\mu\nu}$. Replacing T in the previous equation with the explicit form given by (1.16), (1.17), (1.18) and (1.19), one can identify the elements and construct the metric tensor $(g)_{\mu\nu}$ and its inverse. Its determinant is found to be

$$g = 4B^5\beta^8 \sin^2 3\gamma \, \sin^2\theta \ . \tag{1.27}$$

After carefully performing the calculations suggested by (1.25), one obtains the well-known form of the Hamiltonian derived by Bohr [1]

$$\begin{aligned} H_s \ = \ & -\frac{\hbar^2}{2B}\left[\frac{1}{\beta^4}\,\frac{\partial}{\partial\beta}\,\beta^4\frac{\partial}{\partial\beta} + \frac{1}{\beta^2 \mathrm{sin}3\gamma}\,\frac{\partial}{\partial\gamma}\,\mathrm{sin}3\gamma\frac{\partial}{\partial\gamma}\right. \\ & \left. - \frac{1}{4\beta^2}\sum_\kappa \frac{Q_\kappa^2}{\sin^2\left(\gamma - \kappa\frac{2\pi}{3}\right)}\right] + V \ , \end{aligned} \tag{1.28}$$

with Q_κ the quantum mechanical intrinsic angular momentum operators expressed as differential operators of θ_i:

$$\begin{cases} Q_1 = -i\hbar\left(\mathrm{sin}\psi\dfrac{\partial}{\partial\theta} + \dfrac{\mathrm{cos}\psi}{\mathrm{sin}\theta}\dfrac{\partial}{\partial\varphi} - \dfrac{\mathrm{cos}\theta\mathrm{cos}\phi}{\mathrm{sin}\theta}\dfrac{\partial}{\partial\psi}\right) \\ Q_2 = -i\hbar\left(-\mathrm{cos}\psi\dfrac{\partial}{\partial\theta} + \dfrac{\mathrm{sin}\psi}{\mathrm{sin}\theta}\dfrac{\partial}{\partial\varphi} - \dfrac{\mathrm{cos}\theta\mathrm{sin}\phi}{\mathrm{sin}\theta}\dfrac{\partial}{\partial\psi}\right) \\ Q_3 = -i\hbar\dfrac{\partial}{\partial\psi} \end{cases} \tag{1.29}$$

They are related to $\mathcal{M}_\kappa$ by

$$\mathcal{M}_\kappa = \hbar Q_\kappa \ . \tag{1.30}$$

The differential operators for the kinetic energy correspond to wave functions normalized with respect to the volume element

$$\mathrm{d}\tau = \beta^4 \mathrm{d}\beta \, |\sin 3\gamma| \, \mathrm{d}\gamma \, \sin\theta \mathrm{d}\theta \, \mathrm{d}\phi \, \mathrm{d}\psi \ . \tag{1.31}$$

Next section will deal more closely with solutions of the Bohr Hamiltonian.

1.3 The Confined β-soft Rotor Model

As it was mentioned in the introduction, two approaches to the shape transition regions between vibrator and γ-soft nuclei [19] on one hand, and vibrator and prolate deformed nuclei [20] on the other hand, have been developed by Iachello in the framework of the geometric collective model. The critical point symmetries $E(5)$ and $X(5)$ investigated in these approaches focus on the β degree of freedom and are based on a separation of the β degree of freedom from the γ degree of freedom. They describe nuclei placed at very well defined 'distances', in terms of the $R_{4/2} = E_{4_1^+}/E_{2_1^+}$ ratio, from the benchmarks of nuclear structure: 2.20 and 2.90, respectively, as seen in Fig. 1.2. The parameter free (up to overall scale factors) predictions provided by these symmetries are closely realized in some atomic nuclei [23, 24, 25, 26]. The success of the $E(5)$ and $X(5)$ models has led to the development of numerous extensions involving either no free parameters or a single parameter. We discuss here the confined β-soft (CBS) rotor model [2] which interpolates between $X(5)$ and

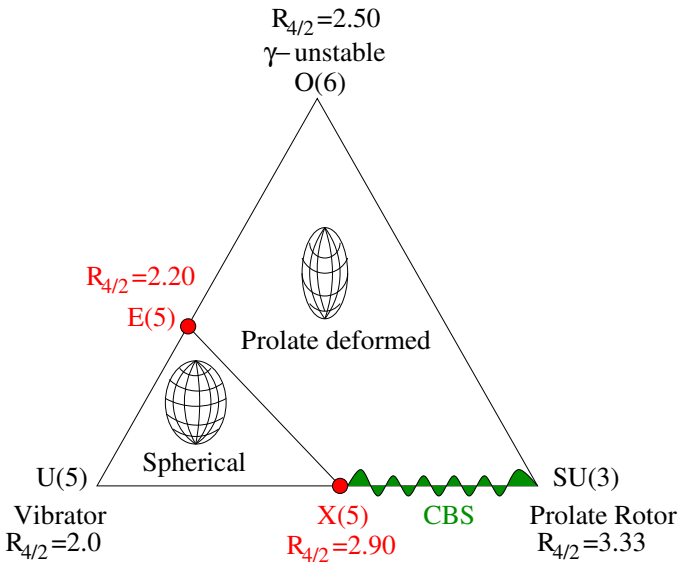

Figure 1.2: *Symmetry triangle, also known as the Casten triangle, of the IBA model. The three dynamical symmetries of the IBA, U(5), O(6) and SU(3), are indicated at the vertices. These correspond to vibrational nuclei with a spherical form [U(5)], axially asymmetric rotors with a flat potential in* γ *[O(6)] and axially symmetric prolate rotors with a minimum at* $\gamma = 0°$ *[SU(3)]. The critical point symmetries E(5) and X(5) occur on the U(5)-O(6) and U(5)-SU(3) legs of the triangle, respectively. An interpolation between X(5) and SU(3) has been achieved in the framework of the CBS model. Most nuclei inhabit the interior of the Casten triangle.*

the rigid rotor $[SU(3)]$ limit (see Fig. 1.2) by using in the $X(5)$ framework infinite square-well potentials in the quadrupole deformation parameter β with boundaries allowed to vary in the range $0 \leq \beta_m \leq \beta \leq \beta_M$. The model contains one free parameter $r_\beta = \beta_m/\beta_M \in [0, 1]$. The limiting case with $r_\beta = 0$ corresponds to the original $X(5)$ model, and $r_\beta \rightarrow 1$ leads to the rigid rotor

$[SU(3)]$ limit. The potential in the γ degree of freedom is assumed to be a harmonic oscillator.

As in [20], we consider the case in which the potential $V(\beta,\gamma)$ in the Bohr Hamiltonian (Eq. 1.28) has a minimum at $\gamma = 0°$. The solutions will be of the form $\Psi(\beta_i) = \varphi_K^L(\beta,\gamma)D_{M,K}^L(\theta_i)$. Around $\gamma = 0°$, the sum in the last term of Eq. (1.28) can be written as

$$\sum_\kappa \frac{Q_\kappa^2}{\sin^2\left(\gamma - \kappa\frac{2\pi}{3}\right)} \simeq \frac{4}{3}\left(Q_1^2 + Q_2^2 + Q_3^2\right) + Q_3^2\left(\frac{1}{\sin^2\gamma} - \frac{4}{3}\right) . \qquad (1.32)$$

With this, the Schrödinger equation becomes

$$\left\{-\frac{\hbar^2}{2B}\left[\frac{1}{\beta^4}\,\frac{\partial}{\partial\beta}\,\beta^4\frac{\partial}{\partial\beta} + \frac{1}{\beta^2\sin3\gamma}\,\frac{\partial}{\partial\gamma}\,\sin3\gamma\frac{\partial}{\partial\gamma} - \frac{1}{4\beta^2}\left(\frac{4}{3}L(L+1)\right.\right.\right.$$
$$\left.\left.\left. +\; K^2\left(\frac{1}{\sin^2\gamma} - \frac{4}{3}\right)\right)\right] + V(\beta,\gamma)\right\}\varphi_K^L(\beta,\gamma) = E\varphi_K^L(\beta,\gamma) . \qquad (1.33)$$

If we now consider potentials $V(\beta,\gamma) = u(\beta) + v(\gamma)$, the wave functions approximately separate into $\Psi(\beta_i) = \xi_L(\beta)\eta_K(\gamma)D_{M,K}^L(\theta_i)$ and Eq. (1.33) can be split into a "radial" (in the shape parameters)

$$\left\{-\frac{\hbar^2}{2B}\left[\frac{1}{\beta^4}\,\frac{\partial}{\partial\beta}\,\beta^4\frac{\partial}{\partial\beta} - \frac{1}{3\beta^2}L(L+1)\right] + u(\beta)\right\}\xi_L(\beta) = E_\beta\xi_L(\beta) , \qquad (1.34)$$

and an "angular"

$$\left\{-\frac{\hbar^2}{2B}\left[\frac{1}{\langle\beta^2\rangle\sin3\gamma}\,\frac{\partial}{\partial\gamma}\,\sin3\gamma\frac{\partial}{\partial\gamma} - \frac{1}{4\langle\beta^2\rangle}K^2\left(\frac{1}{\sin^2\gamma} - \frac{4}{3}\right)\right]\right.$$
$$\left. + v(\gamma)\right\}\eta_K(\gamma) = E_\gamma\eta_K(\gamma) \qquad (1.35)$$

differential equations, where $E = E_\beta + E_\gamma$ and $\langle\beta^2\rangle$ is the average of β^2 over

$\xi(\beta)$. Making the change of variables

$$\begin{cases} z = \sqrt{\frac{2B}{\hbar^2}E}\ \beta & \text{(a)} \\ \\ \tilde{\xi}(z) = \beta^{3/2}\xi_L[\beta(z)] & \text{(b)} \end{cases} \tag{1.36}$$

and by setting

$$\nu = \left[\frac{L(L+1)}{3} + \frac{9}{4}\right]^{1/2} , \tag{1.37}$$

Eq. (1.34) transforms into the Bessel equation

$$\tilde{\xi}'' + \frac{\tilde{\xi}'}{z} + \left[1 - \frac{\nu^2}{z^2}\right]\tilde{\xi} = 0 , \tag{1.38}$$

with solutions the Bessel functions of the first and second kind, $J_\nu(z)$ and $Y_\nu(z)$, respectively, of irrational order ν. The general solutions are a linear combination of the Bessel-J and Bessel-Y functions:

$$\tilde{\xi}_\nu(z) \propto J_\nu(z) + \gamma_Y Y_\nu(z) . \tag{1.39}$$

The boundary conditions imposed by the choice of potential (infinite square-well) require the wave function to vanish outside the well

$$\tilde{\xi}_\nu(z_m) = \tilde{\xi}_\nu(z_M) = 0 . \tag{1.40}$$

With the definition of r_β and Eq. (1.36a), the above conditions become

$$\tilde{\xi}_\nu(r_\beta z_M) = \tilde{\xi}_\nu(z_M) = 0 , \tag{1.41}$$

and they determine the relative amplitude

$$\gamma_Y = \frac{J_\nu(z_M) - J_\nu(r_\beta z_M)}{Y_\nu(r_\beta z_M) - Y_\nu(z_M)} , \tag{1.42}$$

and the quantization condition

$$Q_\nu^{r_\beta}(z_M) = J_\nu(z_M)Y_\nu(r_\beta z_M) - J_\nu(r_\beta z_M)Y_\nu(z_M) = 0 \ . \tag{1.43}$$

For each value of $\nu(L)$ and r_β, the corresponding z_M are obtained as the sth zero, $z_{L,s}^{r_\beta}$, of the function $Q_\nu^{r_\beta}(z)$. The quantum number s counts the number of nodes of the wave function in β for $\beta > \beta_m$. We define as first *beta* excitation the 0_2^+ state with $s = 2$.

The normalization constants $c_{L,s}$ are obtained by imposing the condition

$$\int_{\beta_m}^{\beta_M} \beta^4 \xi_{L,s}^2(\beta) \mathrm{d}\beta = 1 \ . \tag{1.44}$$

Here, the wave functions are normalized with respect to the volume element in the β degree of freedom suggested by Eq. (1.31). Then, the normalized eigenfunctions of Eq. (1.34) are

$$\xi_{L,s}(\beta) = c_{L,s}\beta^{-3/2}\left[J_\nu\left(z_{L,s}^{r_\beta}\frac{\beta}{\beta_M}\right) + \gamma_Y Y_\nu\left(z_{L,s}^{r_\beta}\frac{\beta}{\beta_M}\right)\right] \ , \tag{1.45}$$

with eigenvalues

$$E_{L,s}^{\beta} = \frac{\hbar^2}{2B\beta_M^2}\left(z_{L,s}^{r_\beta}\right)^2 \tag{1.46}$$

and constant

$$c_{L,s} = \left\{\int_{\beta_m}^{\beta_M} \beta\left[J_\nu(z_{L,s}^{r_\beta}\beta/\beta_M) + \gamma_Y Y_\nu(z_{L,s}^{r_\beta}\beta/\beta_M)\right]\mathrm{d}\beta\right\}^{-1/2} \ . \tag{1.47}$$

The parameter $B\beta_M^2$ defines the energy scale. The relative excitation energies depend only on the model parameter r_β. For the ground band we have [27]

$$R_{L/2} = \frac{E_x(L_1^+)}{E_x(2_1^+)} = \frac{\left(z_{L,1}^{r_\beta}\right)^2 - \left(z_{0,1}^{r_\beta}\right)^2}{\left(z_{2,1}^{r_\beta}\right)^2 - \left(z_{0,1}^{r_\beta}\right)^2} \ . \tag{1.48}$$

The solution to equation (1.35) is identical with the one given in [20]. Let $\tilde{v}(\gamma) = \frac{2B}{\hbar^2} v(\gamma)$ and $\epsilon_\gamma = \frac{2B}{\hbar^2} E_\gamma$. With the choice of potential mentioned before, Eq. (1.35) becomes the radial equation of a two dimensional oscillator when one expands in powers of γ

$$\left[-\frac{1}{\langle\beta^2\rangle}\frac{1}{\gamma}\,\frac{\partial}{\partial\gamma}\,\gamma\frac{\partial}{\partial\gamma} + \frac{(K/2)^2}{\langle\beta^2\rangle}\frac{1}{\gamma^2} + (3a)^2\frac{\gamma^2}{2} \right] \eta_K(\gamma) = \tilde{\epsilon}_\gamma \eta_K(\gamma) \ , \tag{1.49}$$

where

$$\tilde{\epsilon}_\gamma = \epsilon_\gamma + \frac{4}{3}\frac{(K/2)^2}{\langle\beta^2\rangle} \ . \tag{1.50}$$

By imposing the normalization condition

$$\int_0^{\pi/3} |\sin 3\gamma|\, \eta^2_{n_\gamma,K}(\gamma) \mathrm{d}\gamma = 1 \ , \tag{1.51}$$

the normalized eigenfunctions of Eq. (1.49) are

$$\eta_{n_\gamma,K}(\gamma) = c_{n,K}\gamma^{|K/2|} e^{-(3a)\gamma^2/2} L_n^{|K|}(3a\gamma^2) \ , \tag{1.52}$$

where $n = (n_\gamma - |K|)/2$ and $L_n^{|K|}$ is a Laguerre polynomial. The eigenvalues are

$$\tilde{\epsilon}_\gamma = \frac{3a}{\sqrt{\langle\beta^2\rangle}}\,(n_\gamma + 1) \ . \tag{1.53}$$

The quantum number n_γ takes the $0, 1, 2, \ldots$ values and is related to the K quantum number as follows

$$n_\gamma = 0 \quad K = 0; \qquad n_\gamma = 1 \quad K = \pm 2; \qquad n_\gamma = 2 \quad K = 0, \pm 4; \quad \ldots \tag{1.54}$$

The values of L in a sequence s, n_γ are determined by K. For $K = 0$, $L = 0, 2, 4, \ldots$ and for $K \neq 0$, $L = K, K+1, K+2, \ldots$ [1].

Combining all results, we obtain the full, properly symmetrized solution to Eq. (1.33) of the form

$$\Psi_{s,n_\gamma,K,L,M}(\beta_i) = \sqrt{\frac{2L+1}{8\pi}}\left[\varphi_{s,n_\gamma,K,L}(\beta,\gamma)D^L_{M,K}(\theta_i) + (-1)^{L+K}\varphi_{s,n_\gamma,-K,L}(\beta,\gamma)D^L_{M,-K}(\theta_i)\right] . \quad (1.55)$$

The difference between this solution and the $X(5)$ solution resides only in the choice of a finite r_β value.

1.3.1 Predictions and Comparisons with Experiment

The structural parameter r_β defines the width of the square-well potential in the β degree of freedom and thus also the stiffness of the nucleus. The wave functions with many nodes or those for states with low angular momentum have larger contributions in the region close to β_m than others. In effect, increasing the value of r_β shifts all levels to higher energy since the potential narrows, but the most affected will be the aforementioned states. For example, in the ground band, which comprises all states with $s = 1$, the energy of the 0^+ state increases the most, followed by the energies of the 2^+, 4^+ states and so on. The $2^+ \rightarrow 0^+$ energy difference shrinks by a larger fraction than the $4^+ \rightarrow 0^+$ difference. Consequently, the $R_{4/2}$ value increases with r_β until the rigid rotor limit with $R_{4/2} = 3.33$ is reached for $r_\beta \rightarrow 1$. For a given angular momentum L, the energy increases strongly with s as r_β increases. Therefore, the ratio $R_{0/2} = E_{0^+_2}/E_{2^+_1}$ strongly increases with r_β and becomes infinite in the limit $r_\beta \rightarrow 1$. This behavior is readily noticed in Fig. 1.3.

For a fixed r_β, the average deformation of the wave function increases with

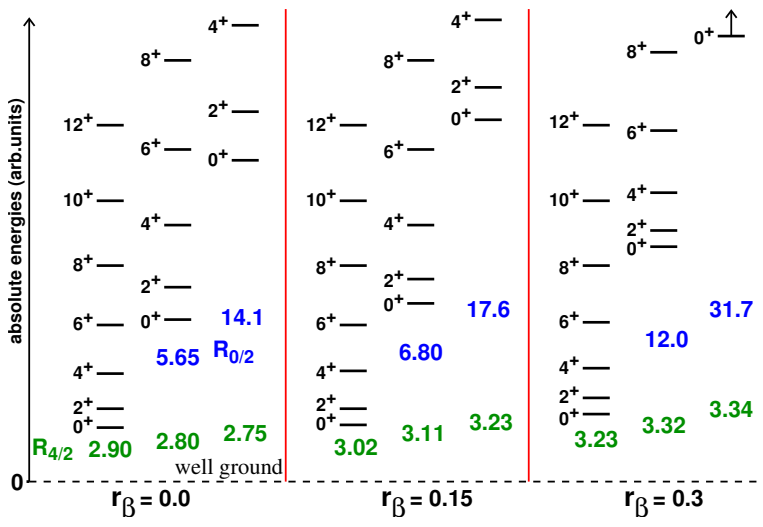

Figure 1.3: *Absolute energies in the CBS rotor model for three widths of the square-well potential. The values of the structural signatures $R_{4/2}$ and $R_{0/2}$ are indicated in green and blue, respectively. The figure was taken from [2].*

increasing angular momentum L, as seen in Fig. 1.4. Over the available range in β, the nucleus gains angular momentum due to centrifugal forces, partially by increasing its rotational moment of inertia rather than its angular velocity. We refer to this phenomenon as *centrifugal stretching*. The effect of stretching attenuates with increasing stiffness of the potential, up to the limit $r_\beta \to 1$, when the nucleus is a rigid rotor and increases its angular momentum solely by angular velocity.

Table 1.1 compares experimental ground state band energies of three transitional nuclei, two Sm isotopes and ^{164}Yb, with predictions of X(5), CBS and Rigid Rotor (RR) models where they are applicable. Since CBS describes the evolution of collectivity between the other two models, we find its predictions for all nuclei while one or the other model fails to give good predictions away

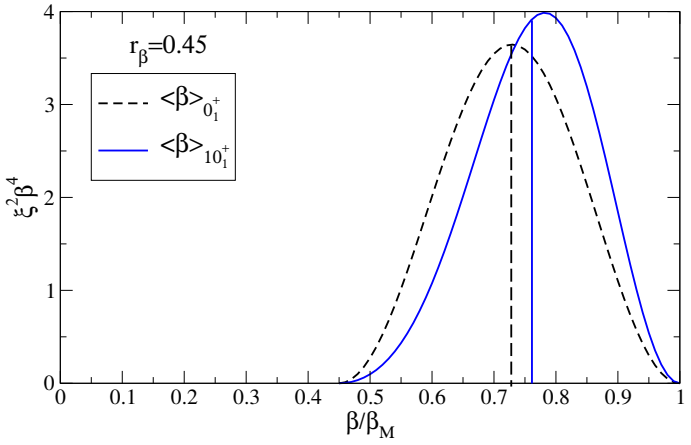

Figure 1.4: *Wave function densities for the* 0^+ *and* 10^+ *states in a potential characterized by* $r_\beta = 0.45$*. The average deformation* $\langle\beta\rangle$ *increases by about 5% from the* 0^+ *to the* 10^+ *state due to centrifugal stretching. The figure was taken from [27].*

from their respective $R_{4/2}$ structural signatures. CBS predicts the energies of each ground state level with less than 5% error, with the accuracy increasing as $r_\beta \rightarrow 1$. It has been demonstrated in [27] that the analytical energy formula of CBS systematically predicts ground state bands (at least up to the 10^+ state) of strongly deformed even-even nuclei in the rare-earth and actinide regions with $R_{4/2} > 3.30$ within a precision of about 1/1000, one to two orders of magnitude more precise than RR.

Model predictions based on energies alone are not enough to validate the CBS model, or for that matter, any other model based on solutions of the Bohr Hamiltonian. An important test for the applicability of the CBS model to transitional and near rigid nuclei is the comparison of its predicted $B(E2)$ with experimental values. The $E(2)$ transition operator for β excitations with

Table 1.1: *Slightly modified version of Table I from [2] with ground state band energies in $^{152,154}Sm$, and ^{164}Yb compared to relevant analytical models, X(5), CBS, and the RR model, where those apply. Structural parameters r_β and signatures $R_{4/2}$ are also given. Neither X(5) nor RR can competitively describe ^{164}Yb with an $R_{4/2}$ value in the middle between the X(5) and the rotor predictions.*

	^{152}Sm			^{154}Sm			^{164}Yb	
J	X(5)	Exp.	CBS	RR	Exp.	CBS	Exp.	CBS
			$r_\beta = 0.14$			$r_\beta = 0.35$		$r_\beta = 0.23$
$R_{4/2}$	2.90	3.01	3.01	3.33	3.26	3.27	3.13	3.13
2_1^+	122	122	122	82	82	82	123	123
4_1^+	354	366	367	273	267	267	386	386
6_1^+	661	707	695	574	544	544	760	753
8_1^+	1033	1125	1093	984	903	901	1223	1202
10_1^+	1465	1609	1554	1503	1333	1325	1753	1723
12_1^+	1954	2149	2077	2131	1826	1810	2330	2315

$n_\gamma = 0$ takes the form [2]

$$T_\mu^{\Delta K=0}(E2) = e_{eff}\left[\frac{\beta}{\beta_M} + \chi\left(\frac{\beta}{\beta_M}\right)^2\right] D_{\mu 0}^2 \ , \tag{1.56}$$

where the effective charge

$$e_{eff} = e^{(1)}\beta_M \left\langle \cos\gamma \right\rangle_\gamma \tag{1.57}$$

and

$$\chi = -\sqrt{\frac{2}{7}} e^{(2)}\beta_M \frac{\left\langle \cos 2\gamma \right\rangle_\gamma}{\left\langle \cos\gamma \right\rangle_\gamma} \tag{1.58}$$

Table 1.2: *Comparison of ground state band $E2$ transition rates in $^{152,154}Sm$ [28, 29] with the X(5) limit and the CBS rotor model for $r_\beta = 0.14$ and 0.35 from Table 1.1. $\chi = -0.535$ was kept constant in the $E2$ operator. The $B(E2)$ values are in Weisskopf units and scales are normalized to the $2_1^+ \to 0_1^+$ transition. This table is a modified version of Table II from [2].*

$J_i^+ \to J_f^+$	X(5)	^{152}Sm	CBS	^{154}Sm	CBS
$2_1^+ \to 0_1^+$	144	144(3)	144	174(5)	174
$4_1^+ \to 2_1^+$	230	209(3)	213	244(6)	251
$6_1^+ \to 4_1^+$	285	245(5)	249	290(8)	281
$8_1^+ \to 6_1^+$	328	285(14)	273	318(17)	300
$10_1^+ \to 8_1^+$	361	320(30)	290	314(16)	314

are free parameters to be adjusted to data. Table 1.2 shows experimental $B(E2)$ values compared to analytical results for X(5) and CBS models. Here too we see good agreement (within the uncertainties up to at least the 10^+) with experiment. The size of the $E2$-transition matrix element is related to the deformation of the intrinsic state, characterized by the intrinsic quadrupole moments Q_0. The reduced transition probability $B(E2)$ is given by [14]

$$B(E2; J_i \to J_f) = \frac{5}{16\pi} e^2 Q_0^2 \left\langle J_i K 20 | J_f K \right\rangle^2 \tag{1.59}$$

where the quantities $\langle J_i K 20 | J_f K \rangle$ are Clebsch-Gordan coefficients. We call the product eQ_0 a transitional quadrupole moment Q_t. In the CBS model we attributed the change in deformation from state to state to centrifugal stretching. A clear way to verify the existence of this phenomenon is to compare the model predictions (calculated by means of Eq. (1.59) from the predicted

$B(E2)$ values) with experimental Q_ts. Figure 1.5 offers such a comparison for two nuclei, ^{152}Sm and ^{172}Yb. Centrifugal stretching is clearly observed for the

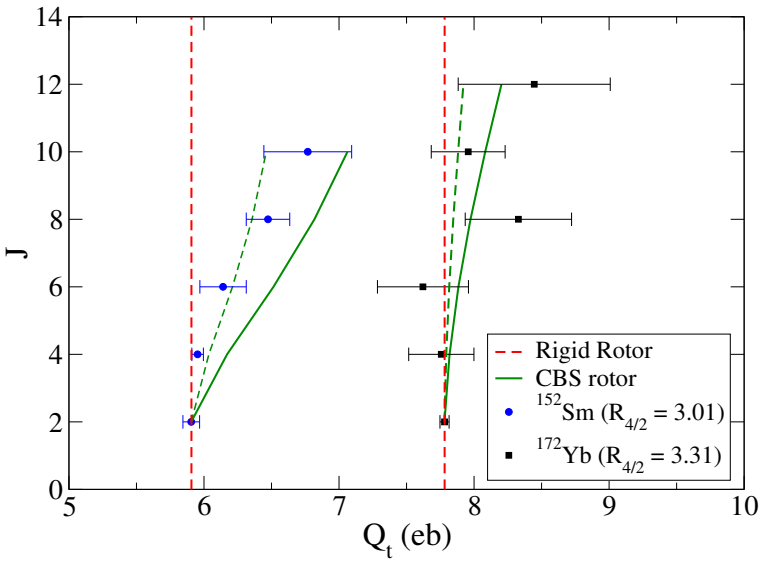

Figure 1.5: *Theoretical and experimental Q_t values as a function of spin, J for ^{152}Sm and ^{172}Yb. The dashed lines represent the rigid rotor prediction while the solid curve is the CBS rotor model prediction with the $E2$ operator in the lowest order in the quadrupole deformation parameter, β ($\chi = 0$, see Eq. (1.56)). Q_t values including a second order correction ($\chi = -0.535$) in the $E2$ operator are represented by the dashed curves. The figure was taken from [27].*

transitional nucleus ^{152}Sm, in good agreement with the CBS prediction using the $E2$ operator up to second order in β. Due to the limit of precision for life-time measurements, observation of the predicted small centrifugal stretching of strongly deformed nuclei with $R_{4/2}$ values of about 3.3, such as ^{172}Yb, is still not possible because the effect to be measured is predicted by the CBS rotor model to be of the same size as the experimental uncertainties. However,

in order to push the observations of centrifugal stretching toward the region of strongly deformed nuclei it would be interesting to extend the precision lifetime information to nuclei with larger stiffness than those near the critical point. This is the intended purpose behind the Thesis work which consisted mainly in performing two experiments on transitional nuclei ^{168,170}Hf using two different timing techniques that will be described in the next chapters.

As closing remarks for this subsection, we note that the interband $E2$ transition strengths are also well predicted [2] by the CBS model. $E0$ transitions can be studied in the CBS. They are predicted to be largest for X(5) and decrease when approaching the rigid rotor limit. For $r_\beta < 1$, $E0$ transitions between two $k = 0$ bands are predicted to decrease with increasing spin.

Chapter 2

Delayed Coincidence Timing

The content of this chapter is largely based on material taken from Ref. [30].

2.1 Introduction

The principle of the delayed coincidence method consists of measuring the distribution of time delays between the formation and subsequent decay of the nuclear state of interest. The time of formation is usually determined by detecting the 'start signal' (γ radiation, β particle, beam pulse) populating the state. The time of decay, the 'stop signal', is marked by the detection of the decay product (γ rays, conversion electrons). The roles of the start and stop signals are often reversed by delaying the pulse which indicates the population of the state under consideration.

2.2 Two-detector Delayed Coincidence Method

The two-detector delayed coincidence method is based on the conventional fast-slow coincidence electronic circuit shown in Fig. 2.1. Beginning from the output of the two detectors D1 and D2, the fast (time) part of the circuit comprises time derivation devices (TDD) and a time-to-amplitude converter, while the slow (energy) part uses main amplifiers (AMP), single-channel analyzers (SCA) and a coincidence analyzer (CA). Common to the two circuits are a linear gate (LG) and a multi-channel analyzer (MCA) or computer. The fast circuit serves for measuring the time difference between any event in detector D1 and any succeeding event in detector D2. Fast pulses coming from detectors are normalized in the TDD. They are then used as start and stop signals for the TAC, which converts the time differences between them to pulse heights in the form of a voltage signal. In the slow circuit, the signals out of D1 and D2 are first amplified and shaped by the main amplifier. The SCA's have to be tuned to the energy windows according to the energies of interest. If the height of the signal from AMP is within the set energy window, a logical signal appears as output. The signals from the two SCA must occur at the same time at the CA if they are physically correlated. If that is the case, a logical signal is generated at exit, which opens the gate of the linear gate stretcher. The TAC signal from the fast circuit is then allowed to pass. A multi-channel analyser or a computer records the amplitude of the TAC signals on the x-axis and their frequency on the y-axis.

If certain conditions are fulfilled in the fast-slow coincidence circuit, acci-

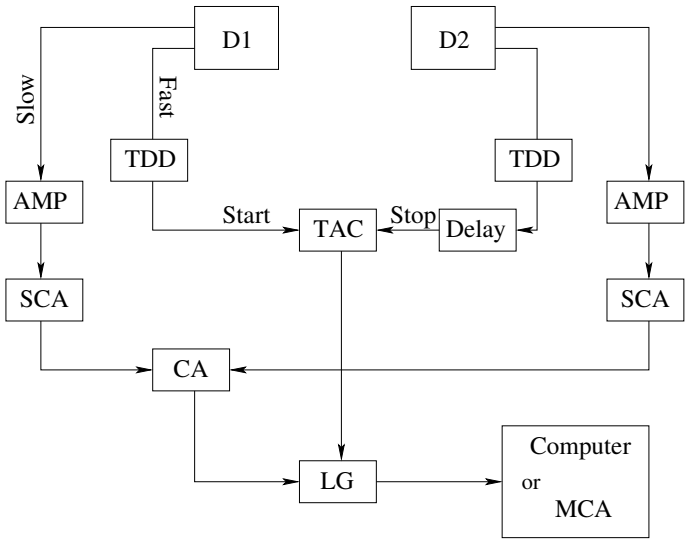

Figure 2.1: *Fast-slow coincidence circuit with two detectors.*

dental coincidences can be measured. They are as follows:

1. the energy condition on D1 set by the SCA must be satisfied;

2. the energy condition on D2 must also be satisfied;

3. the energy conditions 1. and 2. must occur within the time range of the coincidence analyzer;

4. the timing pulses of the two detectors must occur within the range of the TAC.

Based on these conditions, accidental coincidences of *first order* and *higher order* can be distinguished. Accidental coincidences of first order are those for which the timing and the energy pulse of detector D1 is due to an event coming from the decay of one nucleus while the timing and energy pulse of D2 is due to a decay from another nucleus. Thus, the two events are not

correlated, although they originate from the same physical process. Accidental coincidences of first order always fulfill condition 3. if the other conditions are fulfilled. Accidental coincidences of higher order are those for which the timing and energy pulses of one or both detectors do not originate from the same physical process. Thus, condition 3. is an additional requirement for accidental coincidences of higher order.

2.3 Pulsed Beam Method

Nuclear excited states are produced during the beam bursts by nuclear reactions, and the time of the decay of these excited states is observed relative to the time of the beam burst. The shortest lifetime that can be determined with this method is limited by the width of the pulsed beam. The longest lifetime that can be determined by the pulsed beam method depends on the time interval between pulses as it is schematically shown in Fig. 2.2

In this method the time spectra are measured by starting the time analyzer with the pulses from the detector and stopping it with a delayed signal which is synchronized with beam pulses provided by an accelerator. The start and stop signal origins can be in principle exchanged but it would lead to diminished statistics since the counting rate of the detector is usually much lower than the number of beam pulses per second. The advantage of the pulsed beam method compared with the two-detector delayed coincidence method is that one measures essentially a single spectrum since each energy pulse is associated with a time pulse. One can thus obtain good statistics within short measuring

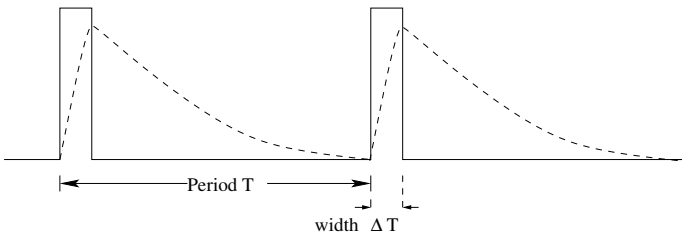

Figure 2.2: *Time distribution of a pulsed beam. The dashed line represents the population and subsequent decay of a state.*

times.

The problems in pulsed beam experiments are that the counts in the prompt time distribution are usually very high and that part of the background is time correlated with the pulsed beam. There is a background which is constant as a function of time, but there is also a background which is caused by the pulsed beam and which is not constant: γ rays and neutrons are produced at the slits before or behind the target and neutrons are produced at the target and some of these may reach the detector between the prompt time peaks of the gamma rays from the target. In this way a non-constant contribution of accidental coincidences to the pulsed beam time spectrum is obtained. They may cause difficulties if one wants to measure lifetimes of states that decay by gamma rays of similar energy.

No time correlated accidental coincidences are observed when measuring delayed coincidences with two detectors using a continuous beam for an in-beam experiment or when making measurements with a radioactive source. The measurements with two detectors are more selective than experiments with a pulsed beam. But to obtain good statistics, the measuring times with

two detectors must be appreciably longer than with the pulsed-beam method.

2.4 Analysis Methods of the Time Spectra

2.4.1 Principle

The experimentally determined time distribution $F(t)$, is the convolution of the prompt time distribution $P(t)$, the experimental time distribution function obtained in the limit $\tau \rightarrow 0$, with an exponential decay curve $f(t)$ having a decay constant λ. $f(t)$ is normalized to the unit area and has the following form

$$f(t) = \begin{cases} \lambda e^{-\lambda t} & \text{for} \quad t \geq 0 \\ \\ 0 & \text{for} \quad t < 0 \end{cases} \tag{2.1}$$

The delayed time spectrum can be expressed as

$$F(t) = \int_0^\infty f(t^{'}) P(t - t^{'}) dt^{'}, \tag{2.2}$$

where the number of counts, F, observed at time t are due to events at time $t^{'}$ that are displaced by the time jitter. Changing the variable to $y = t - t^{'}$ one obtains

$$F(t) = f(t) \int_{-\infty}^{t} e^{\lambda y} P(y) dy. \tag{2.3}$$

Differentiating Eq. (2.3) yields

$$\frac{\mathrm{d}F(t)}{\mathrm{d}t} = \lambda [P(t) - F(t)]. \tag{2.4}$$

It can be observed that for

$$P(t) = F(t) \Rightarrow \frac{\mathrm{d}F(t)}{\mathrm{d}t} = 0, \tag{2.5}$$

which means that the maximum of the delayed time distribution lies on the prompt curve.

2.4.2 Slope Method

Dividing both sides of Eq. (2.4) with $F(t)$ one obtains

$$\frac{\mathrm{d}[\ln F(t)]}{\mathrm{d}t} = -\lambda \left[1 - \frac{P(t)}{F(t)}\right]. \tag{2.6}$$

In the time region where $F(t) \gg P(t)$, Eq. (2.6) becomes:

$$\frac{\mathrm{d}[\ln F(t)]}{\mathrm{d}t} = -\lambda. \tag{2.7}$$

The slope of the straight line obtained by fitting the semilogarithmic plot of $F(t)$ in the part of the measured time spectrum which does not contain the prompt distribution, is the decay constant $\lambda = 1/\tau$. This method of analysis is called the slope method. The applicability of the method is constrained to measurements of lifetimes that are approximately two times longer than the lifetime of the prompt time distribution, provided the prompt contributions from other cascades are not too high. For lifetimes much longer than those of the prompt time distribution, even large prompt contributions do not introduce any systematic errors. The slope method is straightforward because it does not involve any measurements on the prompt time distribution.

2.4.3 Centroid Shift Method

The convolution integral (2.2) yields the lifetime τ as the difference between the first moments (centroids) of the delayed and prompt time distributions [31]:

$$\tau = M_1[F(t)] - M_1[P(t)]. \tag{2.8}$$

In practice, the lifetime information is extracted from a centroid plot versus γ-ray energy, called centroid diagram. The centroids of the prompt gamma transitions form the zero-time line. Deviations of other centroids from the zero-time line are interpreted as an indication of measurable lifetimes. The centroid of a time distribution can be determined with great accuracy. If we assume the time spectrum to have a Gaussian distribution, then the statistical uncertainty of the centroid, C, is given by

$$\Delta C = \frac{\sigma}{\sqrt{N}}, \tag{2.9}$$

where

$$\sigma = 0.4247 \times \text{FWHM} \tag{2.10}$$

is the root mean square deviation and N is the total number of counts recorded in the time spectrum. By means of the centroid shift method, lifetimes much shorter (10-100 times) than the FWHM of the prompt time distribution can be measured.

One of the challenges encountered when employing the centroid shift method is to find prompt transitions close to the γ-ray of interest. This is necessary for a good determination of the difference between the centroid of the delayed transition and the zero-time line. Thus one usually uses two different sources

or targets to obtain the prompt and delayed time distributions. As a result of this procedure, drifts in electronics as a function of time or count rate and differences in source position may introduce systematic errors. Even if the position of the two sources or targets does not differ by more than 0.5 mm, a systematic error of more than 30 ps can be introduced due to the different times at which reactions are produced and gamma rays take to reach the detectors. Experiments with a single source or target eliminate these errors.

Ambiguities in the identification of the radiations feeding and depopulating the level of interest may introduce several errors, especially in experiments involving elements with a complicated level scheme or in-beam where reactions with other materials than the target add to the final spectrum. These ambiguities may involve

1. prompt admixtures from other cascades;
2. delayed admixtures from other cascades;
3. scattering from one detector into another;
4. exchange of populating and depopulating radiation.

It was noticed that the time distributions of the Compton background are somewhat delayed compared with those of prompt photopeaks. This effect is understood to be due to the charge collection process [32, 33]. Lifetime information can be extracted only after carefully eliminating the influence of the Compton background.

In general, when applying the centroid shift method for determination of

lifetimes, one expects that the systematic errors in most experiments are much higher than the statistical errors.

Chapter 3

Recoil Distance Doppler-shift Timing

3.1 Introduction

Doppler shift methods can be used to measure lifetimes of nuclear states in the range $\sim 10^{-9}$ s to $\sim 10^{-14}$ s, which conveniently bridges the gap between direct timing methods and resonance studies in which the width rather than the lifetime is measured. Two different Doppler shift methods were developed, corresponding to the time ranges over which their usage provides a satisfactory accuracy for the measured lifetimes: recoil distance Doppler-shift (RDDS) for the 10^{-9} s to 10^{-12} s interval and Doppler shift attenuation method (DSAM) for the 10^{-12} s to 10^{-14} s interval. The separation time $\sim 10^{-12}$ s of the two methods is given by the characteristic slowing down time of a nucleus in a material. Pioneering experiments using the RDDS method were performed by Devons *et al.* [34, 35] at a time when accelerator and detector technologies were in their infancy. Thus the measurements were very difficult with only a few experimenters venturing into the field at the time. The regular opera-

tion of tandem electrostatic generators in 1959 and the discovery of lithium drifted germanium detectors in 1965 transformed the measurements of nuclear lifetimes by Doppler shift methods into routine ones. The following sections apply to the RDDS method.

3.2 Principle

The excited nuclei are produced at time $t = 0$ by means of fusion-evaporation, Coulomb excitation or transfer reactions in a very thin target. The momentum transferred by the beam to the compound system causes the excited nuclei to recoil out of the target with a mean velocity v along a well-defined but variable distance d. This distance extends between the target foil and a thick stopper in which the recoiling nuclei are stopped in a time 10^{-12} s. The energy of the photons emitted during the flight time $t = d/v$ is given by the Doppler expression

$$E_\gamma = E_0 \left(1 + \frac{v}{c} \cdot \cos\,\theta\right), \tag{3.1}$$

here in the first order in v/c, where E_0 is the energy of the photons emitted at rest, in the stopper, and θ denotes the angle between the direction of the photon emission and the recoil momentum (see Fig. 3.1). The ratio between the number of γ-rays with energy E_0 and those with energy E_γ depends only on time of flight t and the lifetime τ of the decaying state.

Experimentally, one observes a doublet of lines at E_0 and $E_\gamma = E_0 + \Delta E$ having the intensities I_u (stopped or unshifted component) and I_s (flight or shifted component), respectively. The velocity v is directly obtained from the

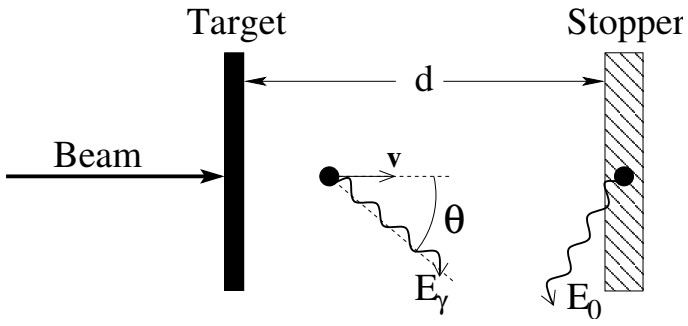

Figure 3.1: *Schematic set-up for an RDDS experiment.*

energy separation of the doublet. The fractional Doppler shift

$$\frac{\Delta E}{E_0} = \frac{v}{c} \cdot \cos\,\theta, \tag{3.2}$$

has to be one order of magnitude greater than the line width $\delta E/E$ of the detectors used, in order to insure a complete separation of the energy doublet, desired for a precise measurement of the stopped and flight intensities and therefore of the lifetime. For comparison, modern day heavy ion induced reactions produce a $v/c \approx 2 - 15 \times 10^{-2}$ while Ge detectors have energy resolutions of $\delta E/E \approx 2 \times 10^{-3}$ making the RDDS method an elegant and precise technique for measuring lifetimes.

A few systematic errors arise due to the intrinsic construction of the method. The most significant error in the analysis of RDDS data is introduced by the time delays of preceding γ-ray emissions from higher-lying states. The effects of feeders can be accounted for if the relative feeding intensities and decay constants are known, although the analysis becomes complicated since complex decay chains have to be integrated.

The deorientation of the nuclear angular momentum under the influence of

hyperfine interactions in ions recoiling into vacuum [40] is a disturbing factor in singles RDDS measurements. The excited nuclei emerge from the target foil at high speeds at which the average ionic charge state $< q >$ can be rather high and inner shell vacancies may be present. The electron rearrangement processes in the freely flying ions involve Auger electron emission and radiative decays and thus can lead to very high and fast changing magnetic hyperfine fields which interact with the magnetic moments of the excited nuclear state under consideration. This hyperfine interaction causes a reduced anisotropy of the γ-ray angular distribution which can even approach isotropy for a long-lived state, and thus introduces an unwanted time dependence of the angular distributions. The γ-ray intensities I_u and I_s taken versus time of flight t appear modified. The deorientation effect introduces corrections in RDDS experiments in heavy nuclei following heavy ion Coulomb excitation to low spin states ($J \leq 6$), but in general it is negligible for light ions and for high spin states populated in heavy ion fusion reactions.

One can avoid these errors if data are recorded in coincidence mode and the analysis is done using the differential decay curve method which will be discussed in a later section of this chapter.

3.3 The Plunger

Although simple and elegant in principle, the RDDS requires a sophisticated device called plunger in order to achieve high precision and to extend the time range to 1 ps. For a typical $v/c \approx 3\%$ of a recoil nucleus, the mean

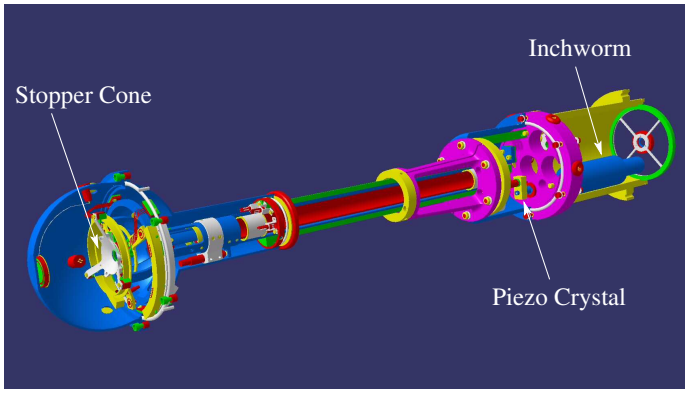

Figure 3.2: *Schematic drawing of the plunger apparatus.*

free path $v\tau$ for an excited level with $\tau \approx 10^{-12}$ s is 10 μm. An accurate determination of such a lifetime requires the stable positioning of the target to stopper down to distances of 1 μm. The first application of a plunger in an RDDS measurement was reported by Alexander and Allen [36]. Since then, various designs have been proposed which optimize the flatness of the target and stopper foils under beam irradiations, the accuracy in adjusting the flight distance d and the integration of the instrument in modern Ge detector arrays with Compton suppression. In this section, the Cologne plunger described in Refs. [37, 38] will be presented.

Fig. 3.2 shows a schematic drawing of the Cologne plunger. The important parts, where visible, are indicated in the figure. The target and stopper foils are first glued on aluminum rings and then stretched by screwing the rings on support holders with conical shapes in the center. The cones determine the plane of the stopper and target. They are well polished around the circular ring at the top to insure flat surfaces for both target and stopper, when screwed into them. The diameter of the central hole of the stopper cone is bigger than that

of the target in order to efficiently capture the recoils. The stretched target and stopper are mounted on frames which are attached to a movable rod and to the fixed body of the plunger, respectively. The target frame can be moved very precisely, through the rod, by a piezoelectric drive (inchworm) which is mounted inside one of the compartments of the plunger under vacuum. The target and the stopper are adjusted parallel to each other by means of three screws.

The plunger has a distance regulation system in action during experiments. This is necessary due to small fluctuations in the beam current or due to the high amount of energy deposited in the target and stopper and the thermal expansion of their materials, all of which can cause significant changes in the distance between foils. For example, bumps with sizes varying from 1 μm to 100 μm, can appear at the beam spot when the beam current exceeds a certain value. The distance regulation system determines the exact separation of the foils by measuring the capacitance C between them. The method was proposed by Alexander and Bell [39]. A step pulse of amplitude V from a pulse generator is applied to the stopper. The target is connected to the input of a charge sensitive amplifier. The capacitance is directly given by

$$C = \frac{Q}{V}, \tag{3.3}$$

where Q is the charge integrated in the amplifier. A distance calibration off-beam is necessary in order to extract a target-to-stopper distance from the measured capacitance C. The target-to-stopper distance d is inversely

proportional to the capacitance C according to the equation

$$C = \epsilon \frac{A}{d}, \tag{3.4}$$

where ϵ is the permittivity of the insulator between the foils and A is the area of each plate. Assuming perfectly flat and exact parallelism of target and stopper foils, a plot of the inverse capacity C^{-1} should linearly go to zero as the separation approaches zero. In practice, due to imperfect alignment and other factors described below, contact is made at some point before the average separation goes to zero. That point will be the effective zero for the micrometer. The expected linearity is observed up from the effective zero,

There are several factors that place an upper limit on the minimum distance between foils. Dust particles sticking on one of the foils will deform them at very small distances (< 20 μm). As a consequence, the measured target-to-stopper capacitance will deviate from the expected one. In the distance calibration, deviations to both larger as well as smaller values can be observed depending on the conductivity of the dust particles. This is a sign of an electrical contact occurring before the mechanical contact. One should avoid measuring at distances where either contact occurs. Another factor is the roughness of the target and stopper materials.

To keep the desired distance fixed during long periods of time, the plunger is equipped with a piezo crystal. It compensates for shifts of the target-to-stopper distances, caused by any of the above mentioned situations. The regulation system is indicated in red in Fig. 3.3. When measuring at a certain distance, the capacitance is read by the method described before at very short

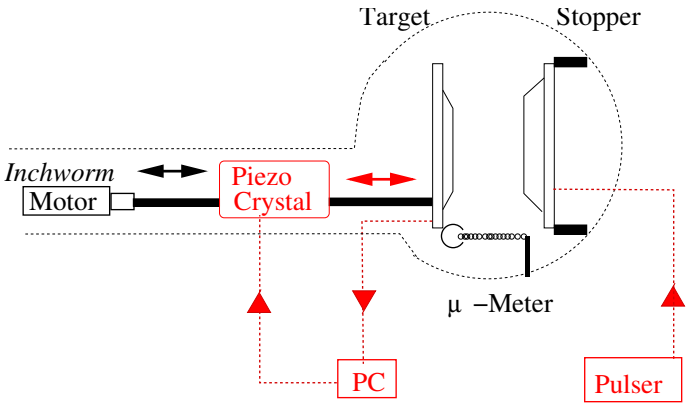

Figure 3.3: *Schematic drawing of the plunger with the distance regulation system components indicated in red.*

time intervals. A computer compares it with the one obtained during the off-beam distance calibration, and any differences are communicated to the piezo crystal only in terms of forward or backward movements, but not in distances. The whole cycle is repeated until the set distance coincides with the measured one.

3.4 Differential Decay Curve Method (DDCM)

3.4.1 General Formulation

The differential decay curve method was proposed in 1989 by Dewald *et al.* [41] and further developed by Böhm *et al.* [42] and P. Petkov [43].

Although there are no problems of principle in the conventional analysis of RDDS data, it turns out that in practice it can become quite difficult. It consists of fitting all observed decay curves by a set of coupled differential

equations after which the individual lifetimes are determined by a χ^2 analysis. In order to obtain a reliable fit, one has to limit the number of free parameters which increases when the excited levels have a complex feeding history. Therefore the intensities of the feeding transitions are usually determined from additional measurements and are kept fixed in the χ^2 fit. If one or more parameters describing the feeding history are not well determined, one may obtain unrealistic lifetimes. Systematic errors are difficult to spot since one can obtain good fits with wrong feeding assumptions.

DDCM replaces the set of coupled differential equations by a single first order differential equation, where the unknown is the lifetime τ of an excited level. All the terms in this equation can be directly obtained from data, if all the feeders of the level of interest are known. To determine this equation, one needs to start with the differential equation which gives the time evolution of population $n_i(t)$ of a state i, fed from higher lying levels h by several transitions and which depopulates by other transitions to lower lying levels j (Fig. 3.4):

$$\frac{\mathrm{d}}{\mathrm{d}t}n_i(t) = -\lambda_i n_i(t) + \sum_h b_{hi}\lambda_h n_h(t), \tag{3.5}$$

where the λ_i, λ_h are the decay probabilities of levels i, h and b_{hi} are the branching ratios of levels h with respect to level i. Integrating Eq. (3.5) one obtains

$$\int_t^\infty \frac{\mathrm{d}}{\mathrm{d}t}n_i(t')\mathrm{d}t' = \int_t^\infty -\lambda_i n_i(t')\mathrm{d}t' + \int_t^\infty \sum_h b_{hi}\lambda_h n_h(t')\mathrm{d}t'. \tag{3.6}$$

Let

$$N_i(t) = \lambda_i \int_t^\infty n_i(t')\mathrm{d}t' \tag{3.7}$$

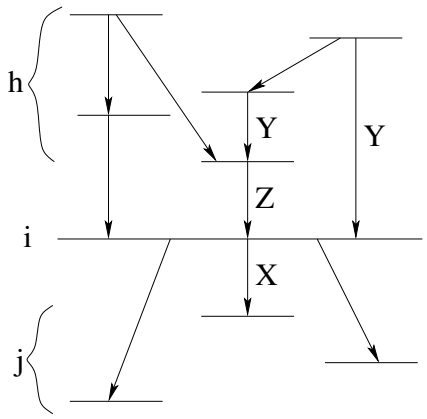

Figure 3.4: *Example of a level scheme where the lifetime of level i is investigated.*

and

$$N_{hi}(t) = b_{hi}\lambda_h \int_t^\infty n_h(t^{'})\mathrm{d}t^{'}. \tag{3.8}$$

Both $N_i(t)$ and $N_{hi}(t)$ are observables of the measurement. The quantity $N_i(t)$ is called the *decay function* of level i. $N_{hi}(t)$ is proportional to function $N_h(t)$ and represents the number of decays $h \rightarrow i$ which occur after flight time t. $N_i(t)$ and $N_{hi}(t)$ are proportional to the unshifted intensities I_u of the γ-transitions $i \rightarrow j$ and $h \rightarrow i$ respectively, measured at flight time t. Similarly, the shifted intensity I_s can be expressed as an integral over $n_i(t)$ in the interval $[0, t)$.

The integration of the left hand side of Eq. (3.6) gives:

$$\int_t^\infty \frac{\mathrm{d}}{\mathrm{d}t} n_i(t^{'})\mathrm{d}t^{'} = n_i(\infty) - n_i(t) = -n_i(t), \tag{3.9}$$

where the assumption that the lifetimes τ_i of level i and of the feeding states

are finite ($n_i(\infty) = 0$) was made. Eq. (3.6) can be written as:

$$-n_i(t) = -N_i(t) + \sum_h b_{hi} N_h(t). \tag{3.10}$$

Observing that the time derivative of Eq. (3.7) is

$$\frac{\mathrm{d}}{\mathrm{d}t} N_i(t) = \lambda_i \left(n_i(\infty) - n_i(t) \right) = -\lambda_i n_i, \tag{3.11}$$

and $\lambda_i = 1/\tau_i$, the basic relationship of DDCM for deriving lifetimes is deduced from Eq. (3.10):

$$\tau_i = \frac{-N_i(t) + \sum_h b_{hi} N_h(t)}{\frac{\mathrm{d}}{\mathrm{d}t} N_i(t)}. \tag{3.12}$$

Eq. (3.12) allows one to calculate the lifetime directly from measured data without the need of a fit procedure, in principle at only three different flight times, $t - \Delta t$, t and $t + \Delta t$. The decay curve of a given level depends strongly on the lifetime of this level only in a certain time interval, called *region of sensitivity*. Lifetime data should be taken mainly at distances in the region of sensitivity. In single measurements, all feeding transitions with significant intensities and their lifetimes have to be known to obtain a reliable lifetime for the level of interest. In case this condition is not fulfilled, one can try to fit the unknown feeding parameters. The best solution for this problem is a coincidence measurement.

3.4.2 DDCM for Coincidence Measurements

For the application of the DDCM to coincidence measurements it has been shown in Ref. [41, 42] how the quantities in Eq. (3.12) can be extracted from the measured data. Only the relevant equations will be presented here.

Two types of coincidences should be distinguished when attempting to find the lifetime of level i in a coincidence measurement:

1. coincidences with depopulating transitions j can be used to reduce the line density in the gated spectra. Coincidences of this type do not help avoiding the problems related to the unknown feeding h, since the feeding pattern of level i is not changed in coincidence with a depopulating transition;

2. coincidences with preceding transitions h take into account only the experimentally observed feeding in the gated spectra. The problem of unknown intensities and lifetimes of unobserved feeding transitions inherent to single measurements is solved. Coincidences with preceding transitions are the main application of the DDCM for coincidence measurements.

The number of events of two simultaneously observed transitions, X and Y, emitted from the same nucleus, are called coincidence intensities and denoted $\{Y, X\}$. The time order of the transitions is included in this notation, with the higher lying and thus earlier occurring transition Y in the first place. In addition, the shifted and unshifted components of a transition are labeled by the subscript s and u respectively. For a level of interest populated indirectly by transition Y and directly by Z and which depopulates by transition X, the lifetime is calculated by

$$\tau(x) = \frac{\{Y_s, X_u\}(x) - \alpha\{Y_s, Z_u\}(x)}{v\frac{\mathrm{d}}{\mathrm{d}x}\{Y_s, X_s\}(x)}, \tag{3.13}$$

where v is the recoil velocity, $x = v \cdot t$ is the target-to-stopper distance, and the factor α is given by

$$\alpha = \frac{\{Y_s, X_u\} + \{Y_s, X_s\}}{\{Y_s, Z_u\} + \{Y_s, Z_s\}}. \tag{3.14}$$

By gating on the shifted component of transition Y, the intensities $\{Y_s, X_s\}$ and $\{Y_s, X_u\}$ can be determined as the peak areas of the two components of transition X. The derivative $\frac{\mathrm{d}}{\mathrm{d}x}\{Y_s, X_s\}(x)$ can be calculated either from the ratio of differences

$$\frac{\mathrm{d}}{\mathrm{d}x}\{Y_s, X_s\}(x_k) = \frac{\{Y_s, X_s\}(x_{k+1}) - \{Y_s, X_s\}(x_{k-1})}{x_{k+1} - x_{k-1}}, \tag{3.15}$$

or by fitting piecewise continuously differentiable second-order polynomials to the measured intensities $\{Y_s, X_s\}(x_k)$. This way it is possible to calculate a value for τ at every distance x, though it does not depend on the target-to-stopper distance at which it was measured. Therefore one expects to measure a constant lifetime τ throughout. Deviations from a straight line in the region of sensitivity of a τ vs x plot point to systematic errors in the analysis. When gates are set on a directly populating γ-ray transition Y, Eq. (3.13) reduces to

$$\tau(x) = \frac{\{Y_s, X_u\}(x)}{v\frac{\mathrm{d}}{\mathrm{d}x}\{Y_s, X_s\}(x)}. \tag{3.16}$$

In summary, the DDCM for the analysis of RDDS coincidence measurements has the following advantages:

1. there are only directly measured coincidence intensities entering into the analysis, no lifetimes or feeding intensities have to be known. The measured lifetimes do not depend on fit parameters;

2. the problem of the unknown feeding is bypassed due to the coincidence measurements and is not specific to the DDCM;

3. only relative distances have to be known in the analysis, therefore the knowledge of the absolute target-to-stopper distance is of no importance;

4. in many cases lifetimes can be obtained without taking into account detector efficiencies and angular distribution factors, reducing the number of possible experimental uncertainties;

5. the statistical uncertainty of the result is considerably reduced by using only gates on the shifted component of the feeding transition;

6. the lifetimes derived are not affected by nuclear deorientation provided the gates are set on transitions which feed directly the level of interest;

7. the τ vs x plot provides an excellent tool for the recognition of systematic errors.

Chapter 4

Experiments

It has been mentioned at the end of Chapter 1 that in order to push the observations of centrifugal stretching toward the region of strongly deformed nuclei it would be interesting to extend the precision lifetime information to nuclei with larger stiffness than those near the critical point, hence our choice of transitional nuclei ^{168,170}Hf. Among nuclei in the rare earth region, ^{168}Hf has an $R_{4/2}$ ratio of 3.11 which is intermediate between the value of 2.90 predicted by the X(5) solution close to the critical point of the shape phase transition and the value of 3.33 for the rigid rotor limit. The CBS rotor model predicts centrifugal stretching of about 8% from the 2_1^+ state to the 10_1^+ state for this nucleus. Precise enough and reliable lifetime information is not available for it. Lifetimes along the ground state band were measured with the RDDS method described in Chapter 3. ^{170}Hf has an $R_{4/2}$ ratio of 3.19 which places it in the region well described by the CBS model, but closer to the RR limit than to the X(5) solution. Due to the intrinsic limitations associated with the timing method used, delayed coincidence, described in Chapter 2, we could

only measure the lifetime of the 2_1^+ state in the ground band. Nevertheless, a more precise determination of this lifetime and thus of the $B(E2; 2_1^+ \rightarrow 0_1^+)$ value is needed for a test of the relevant models and for making more accurate model predictions for $E2$ strengths of higher-lying transitions. Lifetime measurements on the ground band of ^{168,170}Hf were previously done [44] with the RDDS method in singles mode. This method is known to suffer from systematic uncertainties due to unobserved feeding and contaminants.

4.1 The Experiment on ^{168}Hf

4.1.1 Experimental Details

The purpose of the experiment is to measure lifetimes τ along the ground state band in ^{168}Hf. Low spin states of ^{168}Hf were populated using the fusion evaporation reaction ^{124}Sn(^{48}Ti,4nγ)^{168}Hf at the TANDEM facility of WNSL of Yale University. A 190 MeV ^{48}Ti beam bombarded a 1 mg/cm^2 thick ^{124}Sn self-supporting target. Recoiling nuclei were stopped in a 10 mg/cm^2 ^{197}Au stopper. The target and stopper foils were mounted parallel in the New Yale Plunger Device (NYPD). The SPEEDY array was used for γ-ray detection. It consists of 9 segmented CLOVER Ge detectors positioned in 3 groups (rings), where each group (ring) contains only detectors which are positioned at the same angle with respect to the direction of the beam: 1 detector at 0° and 4 detectors at 41.5° in forward position and 4 detectors at 138.5° in backward position. Measurements were performed at 12 different distances between the target and the stopper foils, ranging from 12 μm to 290 μm, for 5 to 11 h each,

necessary in order to be able to determine lifetimes in the interval 1 ps - 50 ps at a $v/c \approx 2\%$ of the recoiling nuclei. $\gamma\gamma$-coincidence matrices were recorded.

4.1.2 Data Analysis

The method used for the analysis of our RDDS data, the differential decay curve method (DDCM), was described in detail in Chapter 3. For each target-to-stopper distance x, 8 matrices were sorted corresponding to the possible combinations of the 3 groups, except for the zero-zero combination, where only one detector is involved. Of the 8 matrices only the 4 corresponding to the forward and backward detectors were used in the analysis. The groups involving the zero degree detector have sensibly less counts than the others, making the determination of peak areas difficult. At a given distance, a lifetime is determined for each group by gating on the shifted component of a direct or indirect feeding transition and measuring the peak areas of the shifted and unshifted depopulating transition or direct populating and depopulating transitions respectively. Lifetimes corresponding to one group but different distances are averaged thus presenting a unique lifetime for the group. The distances selected to provide lifetimes are the ones in the region of sensitivity, which is the time interval, or equivalently the distance interval, where the decay curve of a given level depends the strongest on the lifetime of this level. In practice, these are the distances where the numerator and denominator of Eq. 3.16 are not close to zero. A final lifetime is determined by averaging over the lifetimes provided by each group. Fig. 4.1 shows the gamma-ray spectra of the $6^+ \rightarrow 4^+$ transition obtained at 3 different distances by gating on the

direct feeding transition.

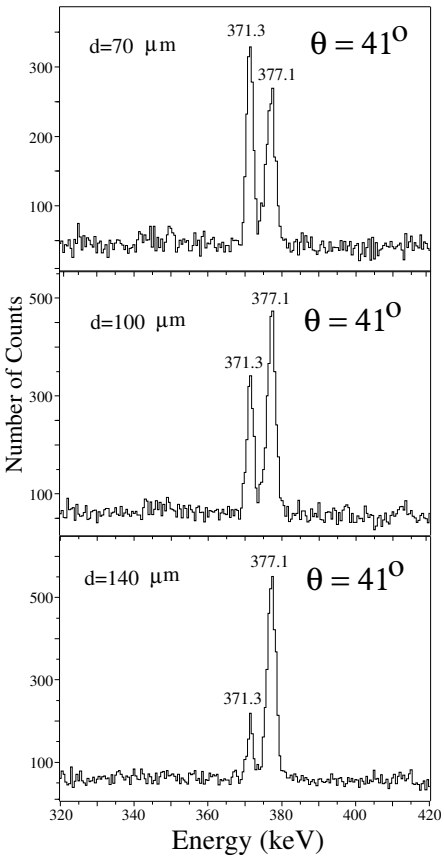

Figure 4.1: *Unshifted and forward shifted components of the* $6_1^+ \rightarrow 4_1^+$ *transition in* ^{168}*Hf at 3 different distances in gated spectra. One can notice the decay pattern on which the RDDS method is based.*

4.1.3 Results

The 4^+ state is populated by a 371.3 keV transition and depopulates by a 261.6 keV transition as can be seen in Fig. 4.2. Gating on the shifted components of the populating transition did not pose any problems so that

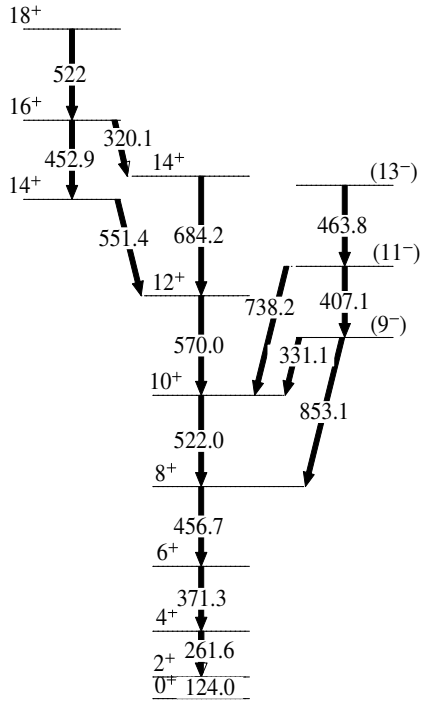

Figure 4.2: *Partial level scheme of* ^{168}*Hf relevant to our analysis. New values for the* 4^+*,* 6^+*,* 8^+ *and* 10^+ *states were obtained.*

we could obtain 4 statistically independent lifetimes corresponding to the 4 groups that were analyzed. They are as follows: 43.9 ± 0.7 ps for the (41.5°, 41.5°) group combination, 44.3 ± 0.6 ps for (138.5°, 138.5°), 42.9 ± 0.6 ps for (41.5°, 138.5°) and 45.7 ± 0.7 ps for (138.5°, 41.5°). As an example, the lifetime obtained for the backward-backward combination is shown in Fig. 4.3. The lifetime of the level is

$$\tau = 44.2 \pm 2.1 \text{ ps.} \tag{4.1}$$

The error is the average of two differences: one calculated by subtracting the average lifetime of the 4 group combinations from the highest lifetime and the

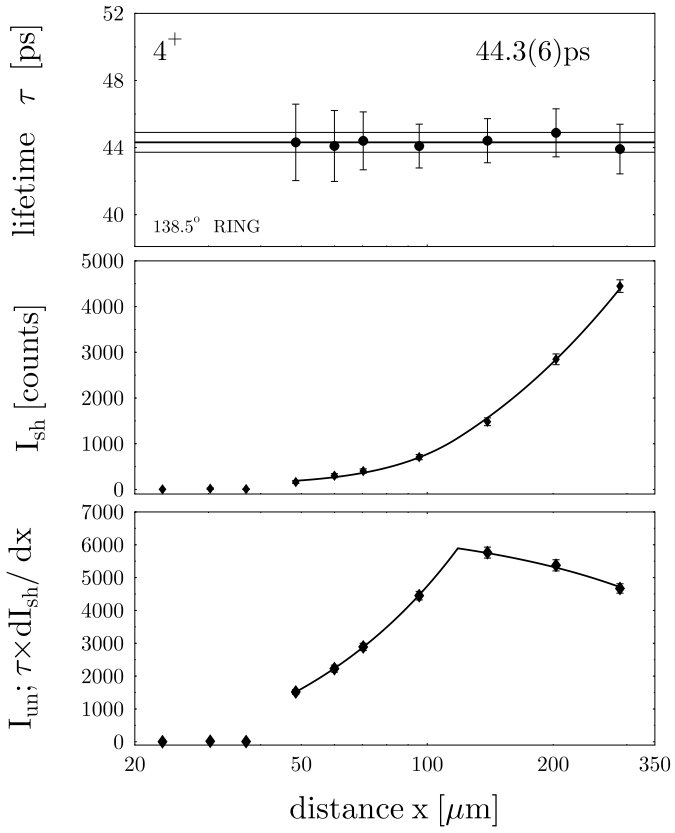

Figure 4.3: *Lifetime of the* 4^+ *state determined in the backward ring. The middle panel shows the shifted intensity at different distances. A continuous curve is fitted through the points in order to calculate the derivative. In the bottom panel, a curve which represents the product between the time derivative of the shifted intensities and the lifetime of the level is compared with the experimental unshifted intensity. Out of this comparison, the lifetimes corresponding to each distance in the region of sensitivity are extracted, as seen in the upper panel.*

other by subtracting the lowest lifetime from the average. Thus it is a maximal error. The corresponding $B(E2; 4_1^+ \rightarrow 2_1^+)$ transition probability is 244 ± 11 W.u.

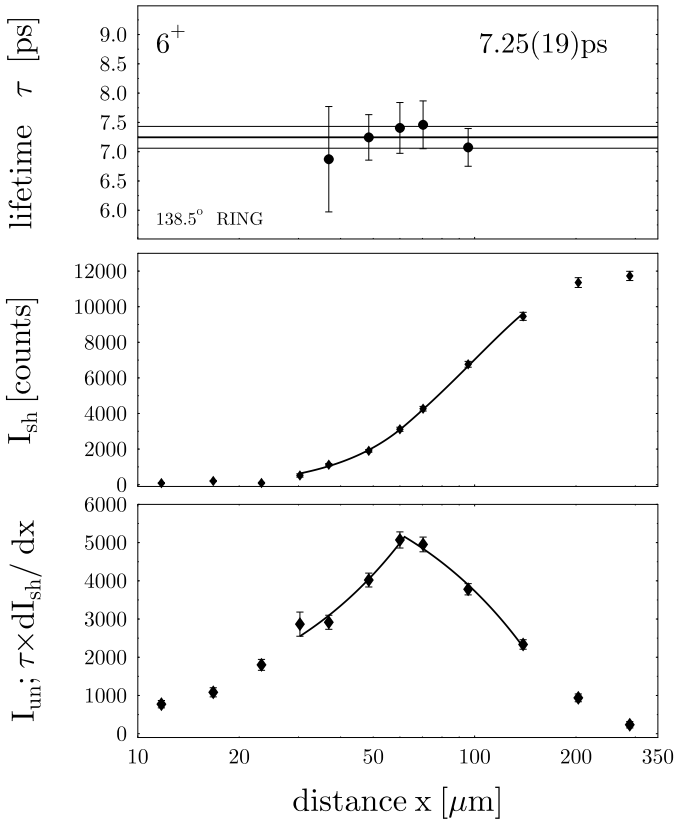

Figure 4.4: *Lifetime of the* 6^+ *state determined in the backward ring. See caption of Fig. 4.3 for further information.*

The 6^+ state is populated by a 456.6 keV transition. Direct gating was possible only in the backward groups due to a contaminant $13^- \rightarrow 11^-$ transition at 463.7 keV which decays on the ground-state band above the 6^+ state and coincides with the forward shifted component of the $8^+ \rightarrow 6^+$ transition.

In addition to direct gating on the directly populating transition we also performed indirect gating on the $14^+ \rightarrow 12^+$ transition at 551.5 keV in order to check the consistency of our results obtained with direct gating. An example is given in Fig. 4.4 in the case of indirect gating from above. The lifetime obtained is

$$\tau = 7.1 \pm 0.4 \text{ ps.} \tag{4.2}$$

We used the same procedure as above for calculating the error. The $B(E2; 6_1^+ \rightarrow 4_1^+) = 283 \pm 17$ W.u.

The 8^+ state is populated by a 522.0 keV transition. It was not possible to gate directly from above due to a $18^+ \rightarrow 16^+$ transition with the same energy located in the ground-state band. We gated indirectly from above on the $12^+ \rightarrow 10^+$ transition. This does not immediately solve the problem of the contaminant because when gating indirectly from above one needs to know the intensities of the shifted and unshifted components of the populating and depopulating transitions of the level of interest (see Eq. (2) and (3)), and the shifted component of the populating transition will still be contaminated by the shifted part of the higher transition. But the unshifted component of the $10^+ \rightarrow 8^+$ transition is not contaminated due to the coincidence requirements we set when gating indirectly from above. We know that all intensity populating the 8^+ level comes from $10^+ \rightarrow 8^+$ 522 keV γ-rays and all depopulating intensity is in the form of $8^+ \rightarrow 6^+$ 456.6 keV γ-rays. The total 522 keV intensity (shifted + unshifted), I^t_{522}, that we measure in the cut spectra is the sum of the shifted, $I^s_{10^+ \rightarrow 8^+}$, and unshifted, $I^u_{10^+ \rightarrow 8^+}$, $10^+ \rightarrow 8^+$ intensity and of the shifted, $I^s_{18^+ \rightarrow 16^+}$, $18^+ \rightarrow 16^+$ intensity. Subtracting from I^t_{522} the total

456.6 keV intensity we obtain $I^s_{18^+\to16^+}$. Finally, the difference between the shifted 522 keV intensity and $I^s_{18^+\to16^+}$ is $I^s_{10^+\to8^+}$. Due to the low number of counts when gating indirectly, we summed the cut spectra obtained by gates at forward and backward groups but with the cut spectra in the same group. Thus we obtained two lifetimes. An example is given in Fig. 4.5. The average

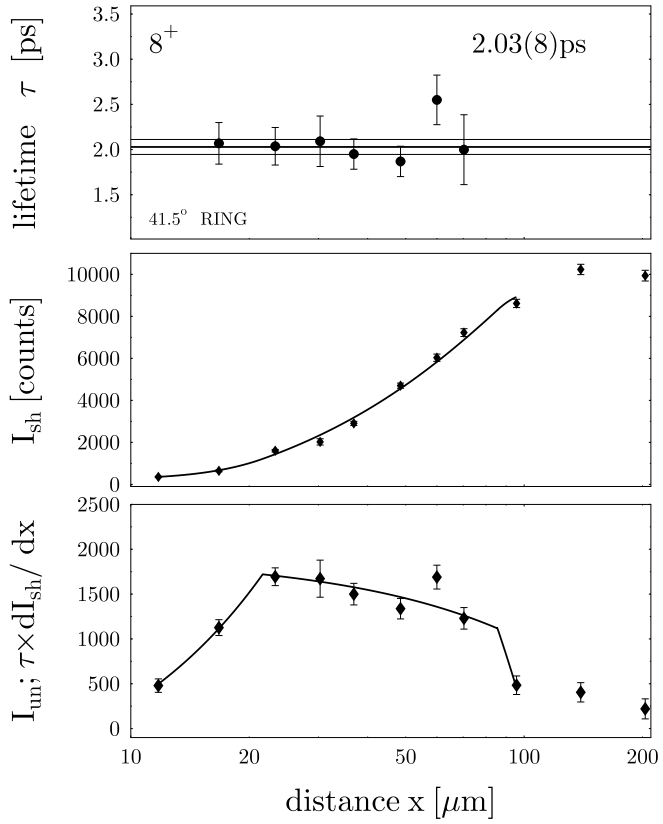

Figure 4.5: *Lifetime of the* 8^+ *state determined in the forward ring. See caption of Fig. 4.3 for further information.*

lifetime is

$$\tau = 2.10 \pm 0.26 \text{ ps} \tag{4.3}$$

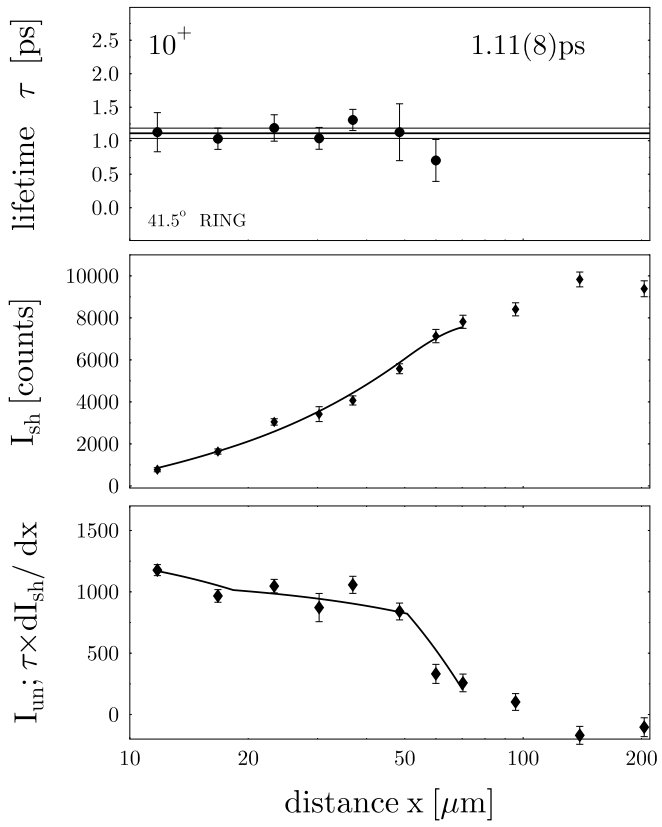

Figure 4.6: *Lifetime of the* 10^+ *state determined in the forward ring. See caption of Fig. 4.3 for further information.*

and the $B(E2; 8_1^+ \rightarrow 6_1^+) = 348 \pm 43$ W.u.

The 10^+ state is populated by a 570.1 keV transition. In this case we gated directly from above and we followed the exact same steps as for the analysis of the 8^+ lifetime since the problem with the $18^+ \rightarrow 16^+$ contaminant was the same. The resulting lifetime and transition probability are

$$\tau = 1.02 \pm 0.14 \text{ ps} \tag{4.4}$$

Table 4.1: *Lifetimes and their corresponding $B(E2)$ transition probabilities along the ground state band in ^{168}Hf. The excitation and transition energies along with the electron conversion coefficients α were taken from [49].*

J	$E(J)$	$E_\gamma(J \to J-2)$	$\tau(J)$	$\alpha(J \to J-2)$	$B(E2; J \to J-2)$	
$\hbar$	keV	keV	ps		e^2b^2	
					this work	Bochev *et al.*[1]
2	124.0	124.0(2)		1.57		0.838(35)
4	385.6	261.6(2)	44.2(21)	0.122	1.344(63)	1.152(116)
6	756.9	371.3(2)	7.1(4)	0.043	1.560(92)	1.300(127)
8	1213.6	456.6(3)	2.10(26)	0.0245	1.91(24)	1.398(132)
10	1735.6	522.0(3)	1.02(14)	0.0175	2.03(28)	1.422(216)

and

$$B(E2; 10_1^+ \to 8_1^+) = 368 \pm 52 \text{ W.u.} \tag{4.5}$$

respectively. An example with the lifetime measured in the forward group is given in Fig. 4.6. Due to Doppler-shift attenuation (DSA) effects in the stopper, the lifetime given above represents a lower limit of the expected lifetime. These DSA effects appear when the lifetime of the level is comparable to the slowing down time of the recoil ^{168}Hf nuclei, which amounts to approximately 1.3 ps. In analysis, this means that some of the intensity we measure in the shifted peaks actually belongs to the unshifted component and the net effect is the lowering of the lifetime. The correction amounts to 10-15% as indicated in Refs. [45] and [46] and it is not necessary for lifetimes greater than 2 ps, at this stopping time. In order to properly account for this effect, one needs to

do a dedicated experiment and to use a DSA analysis method [47] or treat it according to the technique described in Ref. [48], which Refs. [45, 46] follow. A summary of the experimental results is given in Table 4.1. Previous literature values by Bochev *et al.* [44] are also given. We stress that they were obtained in a RDDS measurement in singles mode. The analysis of such data encounters known problems with systematic errors. For the purposes of the discussion we use only our data.

4.2 The Experiment on ^{170}Hf

The contents of this section and of the corresponding discussion, with few modifications, have been published in [50].

4.2.1 Experimental Details

The purpose of the experiment is to measure the lifetime τ of the 2_1^+ state in ^{170}Hf. Low spin states of ^{170}Hf were populated using the ^{158}Gd(^{16}O,4nγ)^{170}Hf fusion evaporation reaction at the TANDEM-LINAC facility of SUNY at Stony Brook. An 80 MeV pulsed ^{16}O beam bombarded a 4.5 mg/cm^2 thick ^{158}Gd target with a 4 mg/cm^2 thick ^{232}Th backing. The pulsed ^{16}O beam with a frequency of 150.4 MHz and a width of about 1.5 ns allows us to measure sub-nanosecond lifetimes [51]. The detection system consisted of two HPGe coaxial detectors and two Low Energy Photon Spectrometer (LEPS) detectors mounted in the Stony Brook cube array [52]. The pulses from the Ge detectors provided the start signals for delayed γ-radiofrequency (rf) coincidences [53].

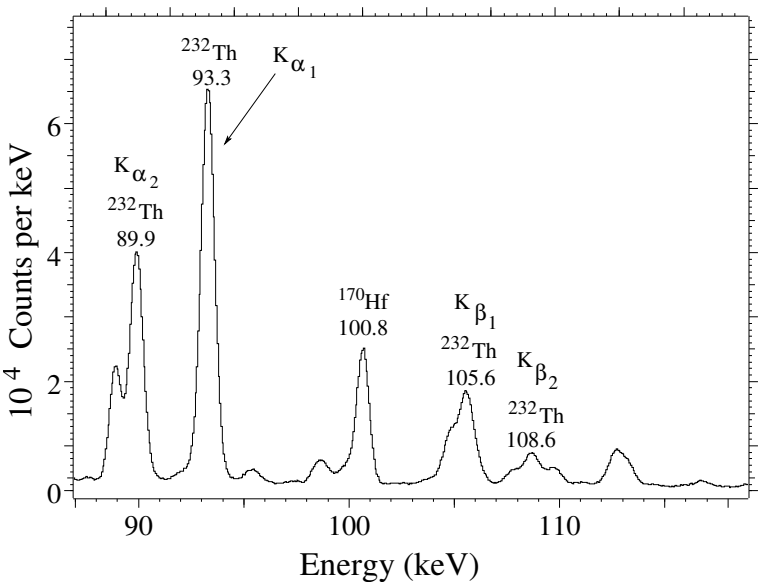

Figure 4.7: *Part of the γ-ray spectrum obtained in the experiment. The x-ray transitions of interest in ^{232}Th and the delayed 100.8-keV $2_1^+ \rightarrow 0_1^+$ transition in ^{170}Hf are labeled.*

Signals synchronized to the LINAC rf were used to stop the time-to-amplitude converter. Smaller values for the time difference $\Delta t_{start-stop}$ between the start and stop signals correspond to γ rays that arrive later at the detector with respect to a prompt γ ray of the same energy. The γ-ray energies as well as their corresponding time difference $\Delta t_{start-stop}$ were recorded and sorted off-line into γ-time matrices. The total number of events collected during the experiment was approximately 10^7 at an average count rate of 2.5 kHz/detector. Sample γ-ray and time spectra are presented in Fig. 4.7 and Fig. 4.8 respectively.

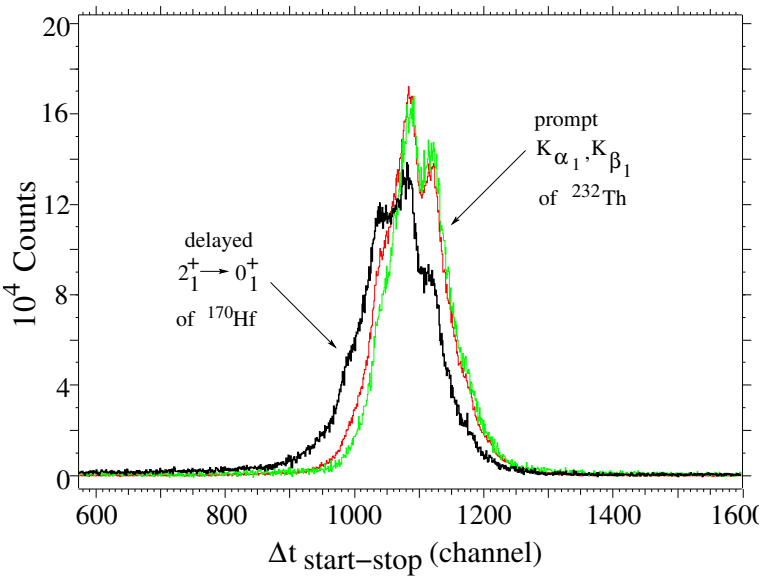

Figure 4.8: *Time difference histograms corresponding to the delayed 100.8-keV* $2_1^+ \rightarrow 0_1^+$ *transition in* ^{170}*Hf (black) and to the prompt 93.3-keV (red) and 105.6-keV (green) x-ray transitions in* ^{232}*Th. The histograms were normalized with respect to the one with maximum integral. Their shape is related to the time structure of the beam bunches.*

4.2.2 Analysis

We use the generalized centroid shift method for data analysis. The principles of the method were described in Chapter 2 and [53]. An experimental improvement with respect to the data analysis described in Ref. [51] resides in the fact that in order to construct the zero-time curve we only used x rays coming from electron capture in the atomic shells of the ^{232}Th backing. The lifetimes of the atomic states that produce these x rays are known to be of the order of femtoseconds. Both the ^{158}Gd target and the ^{232}Th backing were foils

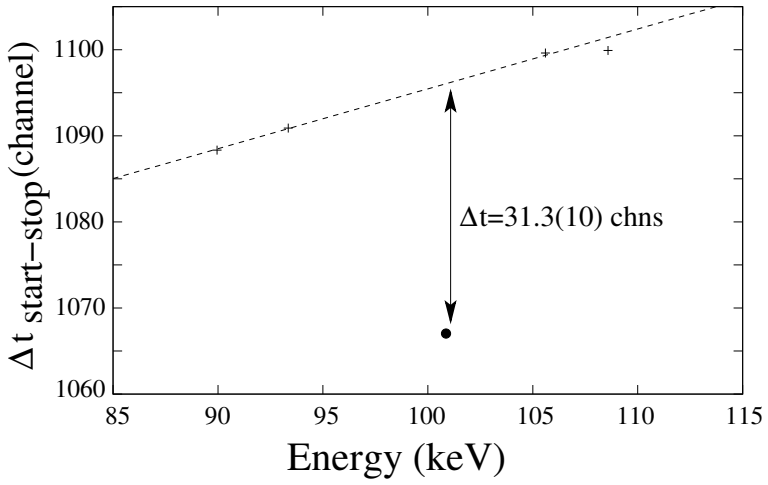

Figure 4.9: *Centroid diagram obtained in the* $^{158}Gd(^{16}O,4n\gamma)^{170}Hf$ *fusion-evaporation reaction for one of the Ge detectors. Crosses represent the centroids of the time distributions of the prompt x-ray transitions. The solid circle represents the data point for the* $2_1^+ \rightarrow 0_1^+$ *transition in* ^{170}Hf*. The radii of the symbols correspond to the statistical errors.*

clamped tightly together by a frame. The zero-time curve was fitted with a linear function as seen in Fig. 4.9. It clearly shows the time delay of the 100.8 keV $2_1^+ \rightarrow 0_1^+$ transition in ^{170}Hf. The observed shift from the zero-time curve amounts to 31.3(10) channels for the example given in Fig. 4.9. The quoted uncertainty includes statistical errors and the uncertainty of our linear fit for the zero-time curve over the short energy interval of interest from 90-110 keV. An additional uncertainty is related to the distance between the target and the ^{232}Th backing assumed to be below 0.1 mm, resulting in an uncertainty of 0.03 ns in the time centroids for the ^{232}Th x rays used for establishing the zero-time curve. The quoted total error also includes this uncertainty.

The time calibration was accomplished by means of shifting the ^{16}O beam bunches in time relative to the oscillator signal of the LINAC by multiples of two r.f. periods (2×6.6489 ns). This beam-skipping procedure yields an accurate result, with an uncertainty in the determination of the slope of the time calibration line smaller than 0.2 ps/ch.

4.2.3 Results

The deviation from the zero-time curve measured for the time centroid of the $2_1^+ \rightarrow 0_1^+$ transition reveals a time delay Δt=1.86(6) ns with respect to the prompt X-rays. This value was obtained from an average over the observed centroid shifts. At this point one has to take into account the effective population time of the level of interest from the levels above it. For the 2_1^+ level, considering all known level lifetimes [49], Δt_{pop}=0.12(1) ns. After correcting for this effect we obtain the 2_1^+ state lifetime

$$\tau = 1.74 \pm 0.06 \text{ ns.} \tag{4.6}$$

The corresponding $B(E2; 2_1^+ \rightarrow 0_1^+)$ transition probability is calculated using

$$\frac{\hbar}{\tau} = (1+\alpha) c_{E2} E_\gamma^5 B(E2; 2_1^+ \rightarrow 0_1^+) \tag{4.7}$$

where α is the electron conversion coefficient. For our case α=3.47, as calculated from the adopted E_γ and pure E2 multipolarity. Then $B(E2; 2_1^+ \rightarrow 0_1^+)$=181 ± 6 W.u.

Chapter 5

Discussion

The data point obtained in the ^{170}Hf experiment is compared to the literature values for the 2_1^+ state of other even-even Hf isotopes in Fig. 5.1. Data on $E2$ transition strengths are available for all nuclei from ^{164}Hf to ^{180}Hf [54]. The 2_1^+ state's excitation energy decreases smoothly to a minimum value at the neutron mid-shell nucleus ^{176}Hf. The $B(E2)$ value almost doubles going from ^{164}Hf, $R_{4/2} = 2.79$, to ^{166}Hf, $R_{4/2} = 2.97$. This, together with the significant drop in $E(2_1^+)$, is interpreted as an increase in $E2$ collectivity of the ground state due to the crossing from the vibrator region, $2.2<R_{4/2}<2.9$, to the rotor region, $2.9<R_{4/2}<3.33$. From ^{168}Hf on, an almost constant $E2$ transition strength is observed. Our new value for ^{170}Hf is close to the maximum values found in ^{174,176}Hf at neutron mid-shell. For ^{174}Hf, the data compilation by Raman, Nestor and Tikkanen [54] reports $B(E2; 2_1^+ \rightarrow 0_1^+)$ values of 182(12) W.u. [55] and 185(12) W.u. [56] from Coulomb excitation conflicting with $B(E2; 2_1^+ \rightarrow 0_1^+)$ values of 158(11) W.u. [57] and 154(9) W.u. [58] from delayed coincidence measurements. Because both pairs have been con-

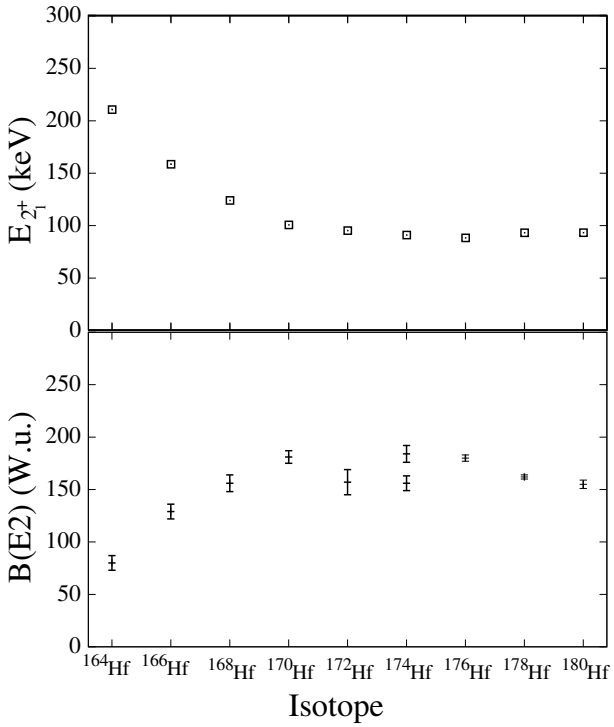

Figure 5.1: $2_1^+ \rightarrow 0_1^+$ *transition energies (top) and corresponding* $B(E2; 2_1^+ \rightarrow 0_1^+)$ *values (bottom) across the Hf isotopic chain. Two conflicting values of* $B(E2)$ *are plotted for* ^{174}*Hf corresponding to Coulomb excitation (top value) and delayed coincidence (bottom value) measurements. Data on Hf isotopes other than* ^{170}*Hf were taken from Ref. [54].*

firmed independently but cannot be right simultaneously, we chose to plot the weighted average of each pair. Because Coulomb excitation is the more direct method for measurements of $B(E2)$ values one might be inclined to favor the higher-lying data point over the lower one. The isotope ^{172}Hf for which the $B(E2; 2_1^+ \rightarrow 0_1^+)$ value has the largest experimental uncertainty, does not seem to follow the smooth trend of data from neighboring isotopes although

the $E(2_1^+)$ energy does. The data point relied entirely on delayed coincidence data from the 1960s [59]. Coulomb excitation of ^{172}Hf has not been done because the nuclide is radioactive. New measurements with higher accuracy would be needed for checking whether an interesting structural effect causes this anomaly or whether the error bars have been underestimated on the data point. Except for the delayed coincidence data on ^{172,174}Hf, the entire data set of even-even Hf isotopes (Z=72) shows the smooth variation expected for fully collective structures with maximum collectivity near neutron mid-shell.

The variation of collectivity seen in the Hf isotopes corresponds to the variation in P factor defined [60] as the average valence proton-neutron interaction, $P = N_p N_n/(N_p+N_n)$. Here N_p (N_n) is the number of proton (neutron) particles or holes outside the nearest shell closure. The P factor is closely correlated to the evolution of nuclear collectivity [60]. Along the Hf isotopic chain the P factor varies from 5.0 (^{164}Hf) to 6.9 (^{176}Hf). It is interesting to compare the data on the Hf chain to those from nuclei that have the same P factor. Our data point on ^{170}Hf corresponds to $P \simeq 6.2$. Fig. 5.2 shows all available data on $E(2_1^+)$ (top) and $B(E2; 2_1^+ \rightarrow 0_1^+)$ (bottom) for even-even nuclei in the rare earth region with $5.9<P<6.5$ and valence neutron particles. It is interesting to note that the data points for $E(2_1^+)$ - with two exceptions discussed below - fall on two constant lines: one line for nuclei with valence proton holes and another one for nuclei with valence proton particles. The 2_1^+ energies in nuclei with valence proton and neutron particles are lower than those in nuclei with valence neutron particles and proton holes. This indicates higher collectivity in particle-particle nuclei as compared to those in the

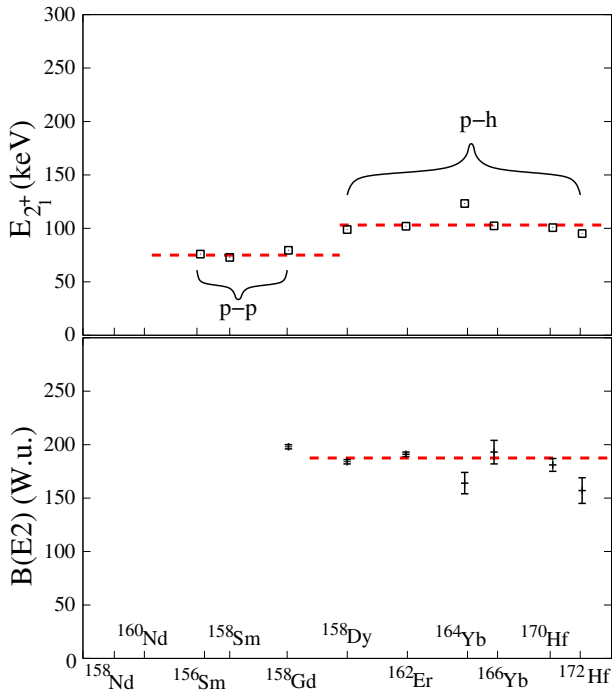

Figure 5.2: $2_1^+ \rightarrow 0_1^+$ *transition energies (top) and corresponding* $B(E2; 2_1^+ \rightarrow 0_1^+)$ *values (bottom) for nuclei with a P parameter of 6.2±0.3 and situated in the p-p (Z=50-66, N=82-104) and p-h (Z=68-82, N=82-104) regions. Data other than the* $B(E2; 2_1^+ \rightarrow 0_1^+)$ *value of* ^{170}*Hf are taken from Ref. [54]. No* $2_1^+ \rightarrow 0_1^+$ *transition energies or* $B(E2; 2_1^+ \rightarrow 0_1^+)$ *values for* ^{158,160}*Nd are known. The* $B(E2; 2_1^+ \rightarrow 0_1^+)$ *values for* ^{156,158}*Sm are also unknown.*

particle-hole region. Valence proton-neutron interaction in nuclei with identical character (particle-particle or hole-hole) stronger than the interaction in nuclei with opposite character (particle-hole) has recently been found to lead to earlier formation of collectivity [61]. This is consistent with the jump in $E(2_1^+)$ values seen at the top of Fig. 5.2. Unfortunately, $B(E2)$ values are not available for ^{158,160}Nd and ^{156,158}Sm to confirm this finding for nuclei with

$P = 6.2 \pm 0.3$ for quadrupole transitions strengths too. Only one data point, the $B(E2; 2_1^+ \rightarrow 0_1^+)$ value of ^{158}Gd, is known to date in the p-p region. The data on the ^{164}Yb and ^{172}Hf nuclei deviate from the constant behavior of their neighbors. ^{164}Yb is less collective [higher $E(2_1^+)$, lower $B(E2; 2_1^+ \rightarrow 0_1^+)$] than other nuclei with the same P. Although the P factor for ^{164}Yb agrees within 5% with the ones of its neighbors, its valence nucleon product N_pN_n deviates by 10% (N_pN_n=144) compared with that of ^{170}Hf (N_pN_n=160). The valence product N_pN_n is known to be an alternative parameter for the evolution of collectivity [62]. It can be used to differentiate the behavior of nuclei with equal P factors. The low value of N_pN_n for ^{164}Yb is consistent with observations. Out of all other nuclei in Fig. 5.2, only ^{156}Sm (-10%), ^{160}Nd and ^{172}Hf (+12.5%) have deviations of the N_pN_n product by more than 5% from that of ^{170}Hf. We already pointed out the case of ^{172}Hf. We further note the lower energy of its 2_1^+ state compared to other p-h nuclei in Fig. 5.2 and its higher N_pN_n product. We expected therefore a $B(E2)$ value slightly higher than those found for the other p-h nuclei in Fig. 5.2. This is not the case. However, the questionable reliability of the literature $B(E2)$ value for ^{172}Hf is discussed above.

A clear way to verify the existence of centrifugal stretching has been introduced in Chapter 1 by means of Q_t plots. Fig. 5.3 shows the predictions of the rigid rotor model and CBS model with E2 operator $T(E2) \propto \beta + \chi\beta^2$ (normalized to the experimental $B(E2; 2_1^+ \rightarrow 0_1^+)$ value) and the experimental Q_t values. Apparently, a precision of the order of the new data point is needed in all values for concluding on the centrifugal stretching of the ^{170}Hf nucleus.

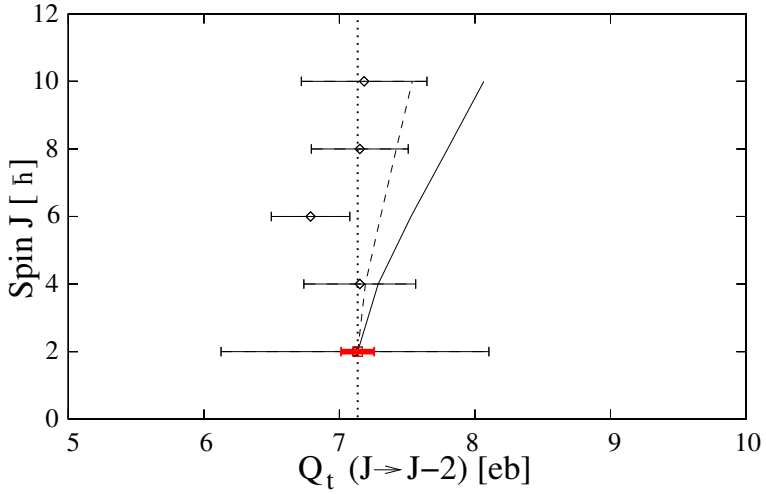

Figure 5.3: *Theoretical and experimental transition quadrupole moments, Q_t, as a function of spin, J, in ^{170}Hf. The dotted line represents the rigid rotor prediction while the solid curve is the CBS rotor model prediction with the $E2$ operator in the lowest order in the quadrupole deformation parameter, β ($\chi = 0$). Q_t values including a second order correction ($\chi = -0.535$ [2]) in the $E2$ operator are represented by the dashed curve. Our experimental $Q_t(2_1^+ \rightarrow 0_1^+)$ (red) is superimposed on the previously known experimental value.*

Nevertheless, the small error ($\approx 3\%$) makes this value sufficiently precise for serving as a normalization parameter for meaningful tests of relevant models. Recently, the precise lifetime measured in the ^{170}Hf experiment has been used for the calculation of the g factor of the 2_1^+ state [63].

In the rigid rotor model the moments of inertia are fixed, they do not change whether the nucleus is spinning slower or faster as seen in Eq. (5.1).

$$E_{RR}(J) = \frac{\hbar^2}{2\theta_{RR}} J(J+1) \ . \tag{5.1}$$

The change in energy is obtained entirely by increasing or decreasing the an-

gular momentum. In the CBS, the level energies in the ground state band are given by the expression

$$E_{\mathrm{CBS}}(J_1^+) = \frac{\hbar^2}{2B\beta_{max}^2}\left[(z_{J,1}^{r_\beta})^2 - (z_{0,1}^{r_\beta})^2\right] \tag{5.2}$$

with $z_{J,s}^{r_\beta}$ being the s-th zero of the parametric combination

$$D_{J,s}^{r_\beta}(z) = J_{\nu(J)}(z)\, Y_{\nu(J)}(r_\beta z) - J_{\nu(J)}(r_\beta z)\, Y_{\nu(J)}(z) \tag{5.3}$$

of first order, $J_\nu(z)$, and second order, $Y_\nu(z)$, Bessel functions of the irrational order $\nu(J) = \sqrt{[J(J+1) - K^2]/3 + 9/4}$. The only structural model parameter $r_\beta = \beta_{\min}/\beta_{\max}$ denotes the ratio of the boundaries of the infinite square well potential $V(\beta)$. In order to interpret the results in terms of variable moments of inertia, we define angular momentum dependent moments of inertia in the spirit of the rotor model by

$$E_{CBS}(J) = \frac{\hbar^2}{2\theta_{CBS}(J)} J(J+1) \tag{5.4}$$

and analogously for the experimental energy

$$E_{exp}(J) = \frac{\hbar^2}{2\theta_{exp}(J)} J(J+1)\ . \tag{5.5}$$

First, we compare the moments of inertia from the CBS rotor model to the experimental ones. In order to become independent on any external scales, all energies were normalized to the excitation energy of the first 2^+ state according to

$$R_\theta(J) = \frac{\theta(J_1^+)}{\theta(2_1^+)}\ . \tag{5.6}$$

A plot of the rigid rotor, CBS and experimental values $R_\theta(J)$ is shown in Fig. 5.4. The agreement between the predictions of the CBS model and experiment

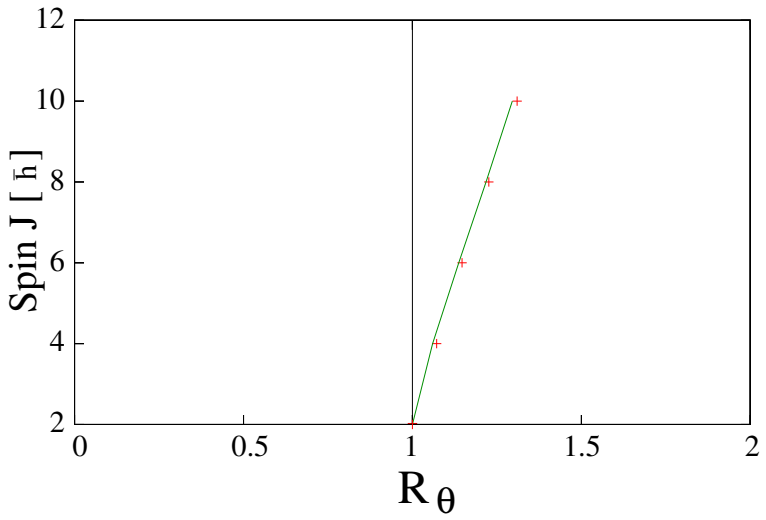

Figure 5.4: *Theoretical and experimental R_θ ratios as a function of spin, J, in ^{168}Hf. The vertical line represents the rigid rotor prediction while the curve is the CBS rotor model prediction with the model parameter $r_\beta = 0.23$.*

is quite satisfactory.

We stress that this agreement between energy data and theory is obtained by sole consideration of a soft potential in β which results in centrifugal stretching as a function of angular momentum. Figure 5.5 shows the wave function densities for the 0_1^+ ground state and the 10_1^+ state obtained from the CBS model as a function of the only model parameter (except for scales), $r_\beta = \beta_{\min}/\beta_{\max}$ (=0.23 for this example). With increasing angular momentum, the center of gravity of the CBS wave functions shift to larger values of deformation $\langle\beta/\beta_{\max}\rangle$. The second column of Table 5.1 lists the values of $\langle\beta/\beta_{\max}\rangle$ from the CBS rotor model for the parameter $r_\beta = 0.23$ obtained from a fit to the energies.

Next it is interesting to see whether the predicted increase of deformation

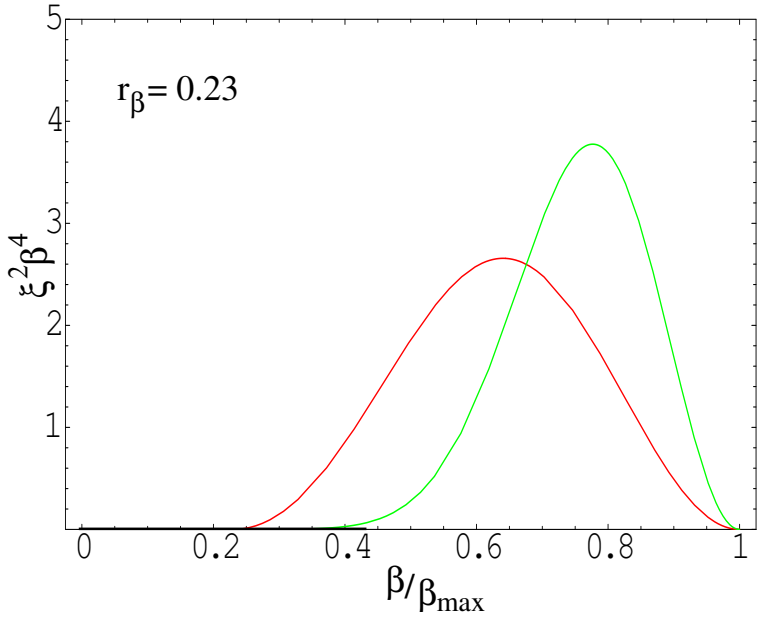

Figure 5.5: *Wave function densities of the* 0_1^+ *and* 10_1^+ *states as a function of deformation, with the model parameter* r_β *set at 0.23. The centers of gravitity of these distributions are given in table 5.1 as* $\langle\beta/\beta_{\max}\rangle(J)$.

with spin is reflected in the data on the $E2$ transition rates. Are the $E2$ data consistent with the conclusions drawn from the energies ? For that purpose we calculate the transitional quadrupole moments (Q_t values) from the model wave functions and from the $E2$ data in the usual fashion

$$Q_t(J_i) = \frac{\sqrt{16\pi}}{\sqrt{5}\langle J_i K 20|J_f K\rangle}\sqrt{B(E2; J_i \to J_f = J_i - 2)}\ . \tag{5.7}$$

The $B(E2)$ values in the CBS rotor model are obtained with the $E2$ operator

$$\hat{T}(E2) = e_{\rm eff}\,\hat{\beta} \tag{5.8}$$

in leading order, only. $Q_t(J)$ is constant in the rigid rotor limit. In order to

Table 5.1: *Average deformations of the wave functions as a function of angular momentum are given in columns 2 and 3 of the table. The absolute fluctuations of these deformations and their relative values are shown in the fourth and fifth columns.*

J	$\langle\beta/\beta_{\max}\rangle(J)$	$\langle\beta\rangle(J)$	$\Delta\beta(J)$	$\Delta\beta/\langle\beta\rangle$
0_1^+	0.631	0.260	0.056	0.217
2_1^+	0.646	0.266	0.055	0.208
4_1^+	0.674	0.277	0.053	0.191
6_1^+	0.704	0.290	0.049	0.170
8_1^+	0.730	0.300	0.046	0.151
10_1^+	0.752	0.309	0.042	0.137

be independent of scales we consider the ratio

$$R_{Q_t}(J) = \frac{Q_t(J_1^+)}{Q_t(2_1^+)} \tag{5.9}$$

for the rigid rotor model, for the CBS model, and for the data. The results are plotted in Fig. 5.6. The experimental values follow the prediction of the CBS model within the present experimental uncertainties. We observe that the CBS rotor model describes both, the variable moment of inertia and the increase of $Q_t(J)$ as a function of spin in ^{168}Hf quantitatively in a purely geometrical way. The geometrical CBS model correctly predicts the increase of quadrupole deformation along the ground state band from a fit to the data on excitation energies that solely involves the concept of centrifugal stretching. The absolute values for the 2_1^+ state of ^{168}Hf, $E_x = 124.0$ keV and $B(E2; 2_1^+ \rightarrow 0_1^+) = 0.838(35)\ e^2\mathrm{b}^2$, yield the scale parameters $\beta_{\max} = 0.41$ and $\hbar^2/B = 7.3$

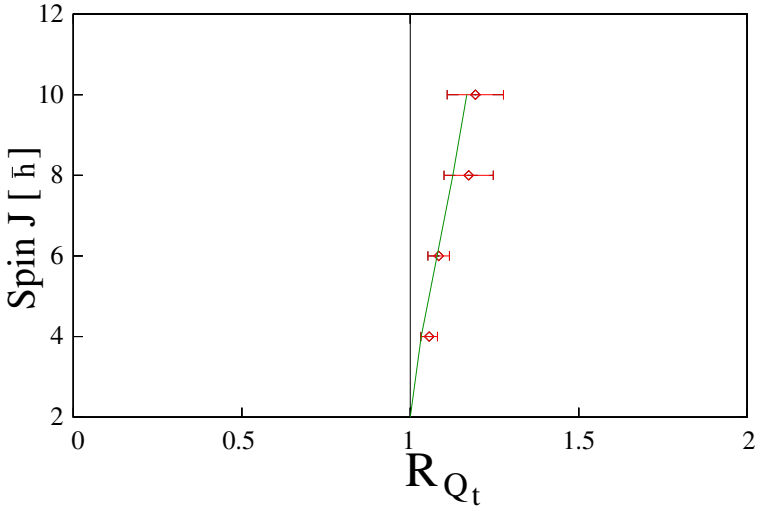

Figure 5.6: *Theoretical and experimental R_{Q_t} ratios as a function of spin, J, in ^{168}Hf. The line represents the rigid rotor prediction while the curve is the CBS rotor model prediction with the $E2$ operator in the lowest order in the quadrupole deformation parameter, β ($\chi = 0$).*

keV. From Figure 5.5 we conclude that the wave functions contain pieces with deformation ranging from $0.23\beta_{\max} = 0.09$ to $\beta_{\max} = 0.41$. Their fluctuations are quite substantial. The absolute fluctuations $\Delta\beta = \sqrt{\langle\beta^2\rangle - \langle\beta\rangle^2}$ and their relative values $\Delta\beta/\langle\beta\rangle$ deduced from the wave functions of the CBS rotor model are shown in the fourth and fifth columns of Table 5.1.

Chapter 6

Conclusions and Outlook

In summary, the lifetime of the 2_1^+ state of ^{170}Hf at 100.8 keV was measured to be $\tau = 1.74 \pm 0.06$ ns, using delayed coincidence timing. This level decays by an $E2$ transition to the 0_1^+ ground state with a transition strength of $B(E2; 2_1^+ \rightarrow 0_1^+) = 181 \pm 6$ W.u. This $E2$ transition rate follows the expected trend of known $B(E2)$ values in isotopic nuclei and empirically confirms the correlation between deformation and the filling of major shells. The small error ($\approx 3\%$) makes this value sufficiently precise to serve as a normalization parameter for meaningful tests of relevant models. Lifetimes of the 4_1^+, 6_1^+, 8^+1 and 10_1^+ ground band states in ^{168}Hf were also measured using recoil distance Doppler-shift timing. The results are consistent with the concept of centrifugal stretching of well deformed nuclei and fit well the CBS rotor model predictions with one parameter r_β.

Fig 5.1 shows an inconsistency between the $2_1^+ \rightarrow 0_1^+$ transition energies and corresponding $B(E2; 2_1^+ \rightarrow 0_1^+)$ values which we thought had to be checked to see whether an interesting structural effect or experimental errors cause it.

We performed experiments on ^{172,174}Hf with the Double Orange Spectrometer [64] at University of Cologne using $e^- - e^-$-coincidence coupled with the pulsed beam technique in order to measure the 2_1^+ state lifetimes. Preliminary results yield $\tau_{2^+} = 1.93(10)$ ns for ^{172}Hf and $\tau_{2^+} = 1.96(8)$ ns for ^{174}Hf corresponding to $B(E2)$ values of 178(9) W.u. and 186(8) W.u., respectively. These new values validate the smooth trend of data indicated by the transition energies. The general result of this Thesis was to push the limit of observations of centrifugal stretching further away on the path from spherical to deformed nuclei. It is highly desired that lifetime measurements on the ground state band be performed on nuclei with an $R_{4/2}$ ratio greater than 3.11. The limit on how close to rigid rotor nuclei we can observe centrifugal stretching is given by the limits in present methods precision. The effects of stretching decrease to about 3.9% change between the $J = 2$ and $J = 10$ states' transitional quadrupole moments for $r_\beta = 0.45$, which roughly corresponds to nuclei with an $R_{4/2} \approx 3.3$.

The CBS rotor model predicts the evolution of the $R_{0/2}$ ratio as a function of the $R_{4/2}$ ratio in a parameter-free way. For nuclei with $2.9 < R_{4/2} \leq 3.2$, the model prediction fits surprisingly well the existing data and points to the fact that the β band, to which the 0_2^+ states belong, in these transitional nuclei has a related collective structure with the ground state band. Still, the energy scale of excited states within the β band is over predicted by the CBS rotor model. This may be due to changes in the pairing interaction in this band relative to the ground state configuration, which are not accounted for in the model. Measurements of the $B(E2; 2_2^+ \rightarrow 0_2^+)$ would help to solve some of

these inconsistencies.

Bibliography

[1] A. Bohr, Mat. Fys. Medd. K. Dan. Vidensk. Selsk. **26**, No. 14 (1952).

[2] N. Pietralla and O. M. Gorbachenko, Phys. Rev. C **70**, 011304(R) (2004).

[3] R. F. Casten, *Nuclear Structure from a Simple Perspective*, second ed., Oxford University Press, New York (2000).

[4] N. Bohr, Nature **137**, 344, 351 (1936).

[5] N. Bohr and F. Kalckar, Mat. Fys. Medd. Dan. Vid. Selsk. **14**, no. 10 (1937).

[6] L. Meitner and O. R. Frisch, Nature **143**, 239 (1939).

[7] N. Bohr and J. A. Wheeler, Phys. Rev. **56**, 426 (1939).

[8] M. G. Mayer, Phys. Rev. **78**, 16 (1950).

[9] J. H. D. Jensen and M. G. Mayer, Phys. Rev. **86**, 1040 (1952).

[10] O. Haxel, J. H. D. Jensen, and H. E. Suess, Zs. f. Physik **128**, 295 (1950).

[11] O. Haxel, J. H. D. Jensen, and H. E. Suess, Ergebn. d. Exakten Wiss. **26**, 244 (1952).

[12] A. Bohr and B. R. Mottelson, Mat. Fys. Medd. Dan. Vid. Selsk. **27**, no. 16 (1953).

[13] A. Bohr and B. R. Mottelson, *Nuclear Structure*, volume I, Benjamin, New York (1969).

[14] A. Bohr and B. R. Mottelson, *Nuclear Structure*, volume II, Benjamin, New York (1975).

[15] F. Iachello and A. Arima, Phys. Lett. B **53**, 309 (1974).

[16] A. Arima and F.Iachello, Phys. Rev. Lett. **35**, 1069 (1975).

[17] A. Arima and F.Iachello, Ann. Phys. (N.Y.) **99**, 253 (1976).

[18] A. Arima and F.Iachello, Phys. Rev. C **16**, 2085 (1977).

[19] F. Iachello, Phys. Rev. Lett. **85**, 3580 (2000).

[20] F. Iachello, Phys. Rev. Lett. **87**, 052502 (2001).

[21] S. S. M. Wong, *Introductory Nuclear Physics*, second edition, Wiley-VCH, Weinheim (2004).

[22] B. Podolsky, Phys. Rev. **32**, 812 (1928).

[23] R. F. Casten and N. V. Zamfir, Phys. Rev. Lett **85**, 3584 (2000).

[24] R. F. Casten and N. V. Zamfir, Phys. Rev. Lett **87**, 052503 (2001).

[25] R. M. Clark, M. Cromaz, M. A. Deleplanque, M. Descovich, R. M. Diamond, P. Fallon, R. B. Firestone, I. Y. Lee, A. O. Macchiavelli, H.

Mahmud, E. Rodriguez-Vieitez, F. S. Stephens, and D. Ward, Phys. Rev. C **68**, 037301 (2003).

[26] R. M. Clark, M. Cromaz, M. A. Deleplanque, M. Descovich, R. M. Diamond, P. Fallon, I. Y. Lee, A. O. Macchiavelli, H. Mahmud, E. Rodriguez-Vieitez, F. S. Stephens, and D. Ward, Phys. Rev. C **69**, 064322 (2004).

[27] K. Dusling and N. Pietralla, Phys. Rev. C **72**, 011303(R) (2005).

[28] N. V. Zamfir, R. F. Casten, M. A. Caprio, C. W. Beausang, R. Krcken, J. R. Novak, J. R. Cooper, G. Cata-Danil, and C. J. Barton, Phys. Rev. C **60**, 054312 (1999).

[29] C. W. Reich and R. G. Helmer, Nucl. Data Sheets **85**, 171 (1998).

[30] W. D. Hamilton, *The Electromagnetic Interaction in Nuclear Spectroscopy*, North-Holland, Oxford (1975).

[31] Z. Bay, Phys. Rev. **77**, 419 (1950).

[32] M. G. Strauss and R. N. Larsen, Nucl. Instr. and Meth. 56, 80 (1967).

[33] D. C. S. White and W. J. McDonald, Nucl. Instr. and Meth. 115, 1 (1974).

[34] S. Devons, G. Manning, and D. St. P. Bunbury, Proc. Phys. Soc. **A68**, 18 (1955).

[35] S. Devons, G. Manning, and J. H. Towle, Proc. Phys. Soc. **A69**, 165 (1956).

[36] T. K. Alexander and K. W. Allen, Can. J. Phys. 43, 1563 (1965).

[37] A. Dewald, P. Sala, R. Wrzal, G. Böhm, D. Lieberz, G. Siems, R. Wirowski, K. O. Zell, A. Gelberg, P. von Brentano, P. Nolan, A. J. Kirwan, P. J. Bishop, R. Julin, A. Lampinen, and J. Hattula, Nucl. Phys. **A545**, 822 (1992).

[38] R. Krücken, A. Dewald, G. Böhm, P. Sala, J. Altmann, K. O. Zell, P. von Brentano, S. A. Forbes, S. M. Mullins, D. J. Thornley, A. J. Kirwan, P. J. Nolan, P. H. Regan, and R. Wadsworth, Nucl. Phys. **A589**, 475 (1995).

[39] T. K. Alexander and A. Bell, Nucl. Instr. Meth. **81**, 22 (1970).

[40] G. Goldring, in: *Heavy Ion Collisions*, 484, North-Holland, Amsterdam (1982).

[41] A. Dewald, S. Harissopulos, and P. von Brentano, Z. Phys. **A334**, 163 (1989).

[42] G. Böhm, A. Dewald, P. Petkov, and P. von Brentano, Nucl. Instr. Meth. **A329**, 248 (1993).

[43] P. Petkov, Nucl. Instr. Meth. **A349**, 289 (1994).

[44] B. Bochev, S. Iliev, R. Kalpakchieva, S. A. Karamian, T. Kutsarova, E. Nadjakov, and Ts. Venkova, Nucl. Phys. **A282**, 159 (1977).

[45] B. Saha, A. Dewald, O. Möller, R. Peusquens, K. Jessen, A. Fitzler, T. Klug, D. Tonev, P. von Brentano, J. Jolie, B. J. P. Gall, and P. Petkov, Phys. Rev. C **70**, 034313 (2004).

[46] O. Möller *et al.*, Phys. Rev. C **74**, 024313 (2006).

[47] G. Böhm, A. Dewald, P. Petkov and P.von Brentano, Nucl. Instrum. Methods Phys. Res. A **329**, 248 (1993).

[48] P. Petkov, D. Tonev, J. Gableske, A. Dewald, and P. von Brentano, Nucl. Instrum. Methods Phys. Res. A **437**, 274 (1999).

[49] National Nuclear Data Center, Brookhaven National Laboratory, *http://www.nndc.bnl.gov/* (2006).

[50] A. Costin, T. Ahn, B. Bochev, K. Dusling, T. C. Li, N. Pietralla, G. Rainovski, and W.Rother, Phys. Rev. C **74**, 067301 (2006).

[51] A. Costin, N. Pietralla, T. Koike, C. Vaman, T. Ahn, and G. Rainovski, Phys. Rev. C **72**, 054305 (2005).

[52] R. M. Wirowski, dissertation, University of Cologne, 1993.

[53] W. Andrejtscheff, M. Senba, N. Tsoupas, Z.Z. Ding, P. Raghavan, Nucl. Instrum. Methods **204**, 123 (1982).

[54] S. Raman, C. W. Nestor, JR., and P. Tikkanen, Atomic Data and Nuclear Data Tables **78**, 1 (2001).

[55] J. Bjerregaard, B. Elbek, O. Hansen, and P. Salling, Nucl. Phys. **44**, 280 (1963).

[56] H. Ejiri and G. B. Hagemann, Nucl. Phys. **A161**, 449 (1971).

[57] H. Abou-Leila, N. N. Perrin, and J. Valentin, Arkiv Fysik **29**, 53 (1965).

[58] A. Charvet, Do Huu Phuoc, R. Duffait, A. Emsallem, and R. Chery, J. Phys. (Paris) **32**, 359 (1971).

[59] H. Abou-Leila, Ann. Phys. (Paris) **2**, 181 (1967).

[60] R. F. Casten, D. S. Brenner, and P. E. Haustein, Phys. Rev. Lett. **58**, 658 (1987).

[61] R. B. Cakirli and R. F. Casten, Phys. Rev. Lett. **96**, 132501 (2006).

[62] R. F. Casten, Nucl. Phys **A443**, 1 (1985).

[63] A. Wolf, Z. Berant, A. Heinz, V. Werner, E. A. McCutchan, G. Gürdal, R. B. Cakirli, Y. Oktem, J. Ai, L. Amon, C. W. Beausang, D. S. Brenner, R. F. Casten, R. J. Casperson, K. Dusling, C. R. Fitzpatrick, A. B. Gransworthy, N. Pietralla, J. Qian, P. H. Regan, N. J. Thompson, E. Williams, and R. Winkler, Phys. Rev. C **76**, 047308 (2007).

[64] Jean-Marc Régis, dissertation, University of Cologne, 2007.